nature communications

Article

https://doi.org/10.1038/s41467-024-55751-4

Inhalable nanovesicles loaded with a STING agonist enhance CAR-T cell activity against solid tumors in the lung

Received: 27 March 2024

Accepted: 23 December 2024

Published online: 02 January 2025

Check for updates

Tianchuan Zhu[1,4], Yuchen Xiao[1,4], Zhenxing Chen[1], Hanxi Ding[1], Shoudeng Chen[2] ✉, Guanmin Jiang[3] ✉ & Xi Huang[1] ✉

Suppression of chimeric antigen receptor-modified T (CAR-T) cells by the immunosuppressive tumor microenvironment remains a major barrier to their efficacy against solid tumors. To address this, we develop an anti-PD-L1-expressing nanovesicle loaded with the STING agonist cGAMP (aPD-L1 NVs@cGAMP) to remodel the tumor microenvironment and thereby enhance CAR-T cell activity. Following pulmonary delivery, the nanovesicles rapidly accumulate in the lung and selectively deliver STING agonists to PD-L1-overexpressing cells via the PD-1/PD-L1 interaction. This targeted delivery effectively avoids the systemic inflammation and poor cellular uptake that plague free STING agonists. Internalized STING agonists trigger STING signaling and induce interferon responses, which diminish immunosuppressive cell populations such as myeloid-derived suppressor cells in the tumor microenvironment and promote CAR-T cell infiltration. Importantly, the anti-PD-L1 single chain variable fragment on the nanovesicle surface blocks PD-L1 upregulation induced by STING agonists and prevents CAR-T cell exhaustion. In both orthotopic lung cancer and lung metastasis model, combined therapy with CAR-T cells and aPD-L1 NVs@cGAMP potently inhibits tumor growth and prevents recurrence. Therefore, aPD-L1 NVs@cGAMP is expected to serve as an effective CAR-T cell enhancer to improve the efficacy of CAR-T cells against solid tumors.

Chimeric antigen receptor (CAR) T-cell therapy has emerged as a revolutionary approach for cancer immunotherapy[1]. By genetically engineering patient-derived T cells to express synthetic CARs, this technology empowers T cells with enhanced capacities to recognize and eliminate tumor cells expressing tumor-associated antigens[2,3]. Currently, CAR-T cell therapy has achieved great success in treating hematologic malignancies[2,4]. However, its effectiveness in solid tumors remains limited due to the immunosuppressive tumor microenvironment (TME)[5–7]. This environment, characterized by anti-inflammatory cytokines, tumor metabolites, and immunosuppressive cells, creates conditions that impede the proliferation and antitumor activity of CAR-T cells.

Reversing the immunosuppressive TME to an immunostimulatory state is thus considered a promising strategy to improve the efficacy of CAR-T cells against solid tumors[8–10]. Studies have shown that pre-treatment of tumor tissue with photothermal agents, immune

[1]Center for Infection and Immunity, Guangdong Engineering Research Center of Molecular Imaging, The Fifth Affiliated Hospital of Sun Yat-sen University, Zhuhai 519000 Guangdong, China. [2]Guangdong Engineering Research Center of Molecular Imaging, The Fifth Affiliated Hospital of Sun Yat-sen University, Zhuhai 519000 Guangdong, China. [3]Department of Clinical laboratory, The Fifth Affiliated Hospital of Sun Yat-sen University, Zhuhai, Guangdong 519000, China. [4]These authors contributed equally: Tianchuan Zhu, Yuchen Xiao. ✉e-mail: chenshd5@mail.sysu.edu.cn; jianggm3@mail.sysu.edu.cn; huangxi6@mail.sysu.edu.cn

checkpoint inhibitors, or other immune activators can partially reverse the suppressive state, thereby enhancing the tumor-killing potential of CAR-T cells[11–16]. Additionally, biomaterials such as lyophilized lymph nodes, lymph node-mimetic scaffolds, and injectable hydrogels can serve as delivery vehicles for CAR-T cells, providing a pro-inflammatory environment in vivo that promotes CAR-T cell proliferation and antitumor activity[17–19]. Notably, activators of the interferon (IFN) gene stimulator (STING) pathway, known for its ability to induce antitumor immunity, have garnered significant interest[20–23]. Through inducing the production of proinflammatory cytokines such as type I interferons and chemokines, STING agonists promote the recruitment of innate and adaptive immune cells, while concurrently restricting the accumulation of immunosuppressive cells such as regulatory T cells (Tregs) and myeloid-derived suppressor cells (MDSCs) within tumors[24–26]. Nonetheless, employing STING agonists to reverse the suppressive tumor microenvironment and enhance CAR-T cell efficacy in solid tumors faces several challenges[27–30]. First, STING agonists are susceptible to degradation by deoxyribonucleases (DNases) and phosphatases in the bloodstream, and their high hydrophilicity hampers their cellular membrane penetration, resulting in suboptimal cellular uptake[26]. Second, given the ubiquitous expression of STING across various cell types, intravenous administration could trigger an overactive immune response, leading to a cytokine storm[24]. While intratumoral administration has been explored, it is not feasible for deep-seated tumors such as lung cancer. Finally, STING agonists can induce the upregulation of programmed death ligand 1 (PD-L1) on tumor cells, which may lead to T-cell exhaustion[23]. Therefore, there is an urgent need to develop efficient delivery systems for STING agonists and strategies to inhibit PD-L1 on tumor cells, thereby improving the antitumor efficacy of CAR-T cells.

Cell membrane-derived nanovesicles are multifunctional drug delivery vehicles owing to their excellent biocompatibility and cargo capacity[31,32]. Furthermore, advances in genetic engineering have enabled the design of nanovesicles with enhanced targeted drug delivery capacities[33–36]. For instance, our team has successfully engineered nanovesicles with improved tumor-targeting properties, significantly enhancing the delivery efficiency of chemotherapeutic agents, photothermal agents, and glutamine antagonists[37–40]. Importantly, these engineered nanovesicles can block immune checkpoints on tumor cells akin to monoclonal antibodies, thus preventing T-cell exhaustion[37,38]. However, intravenously injected nanovesicles tend to accumulate predominantly in the liver, limiting their efficacy against extrahepatic cancers[41]. Fortunately, studies by our team and others have indicated that nebulized administration enables exosomes to primarily accumulate in the lungs, significantly improving the bioavailability of the encapsulated drug in pulmonary tissue[42]. Hence, we hypothesized that inhaled nanovesicles loaded with STING agonists could effectively deliver these agonists to lung tissue, thereby reversing the immunosuppressive TME in lung cancer.

In this study, we developed an anti-PD-L1-expressing nanovesicle loaded with a STING agonist (aPD-L1 NVs@cGAMP) to enhance CAR-T cell potency against solid tumors (Fig. 1). Following inhalation, aPD-L1 NVs@cGAMP rapidly accumulated in lung tissues and delivered cGAMP to cells with high PD-L1 expression in tumor tissues via PD-1/PD-L1 interactions. Once internalized, the STING agonist promotes CAR-T cell infiltration into tumor tissue by inducing proinflammatory cytokines such as IFN-β and chemokines, while simultaneously reducing immunosuppressive cell populations such as MDSCs. Importantly, aPD-L1 NVs@cGAMP effectively prevent CAR-T cell exhaustion in tumor tissues by blocking PD-L1. In mouse models of lung cancer (both primary and metastatic) and tumor recurrence, these nanovesicles substantially enhanced the proliferation and antitumor efficacy of CAR-T cells by remodeling the immunosuppressive TME, thereby improving the survival rate of tumor-bearing mice. Taken together, this study establishes a safe and effective strategy to augment the antitumor potential of CAR-T cells by remodeling the immunosuppressive TME, providing insights into their application against solid tumors.

Results

Preparation and characterization of MSLN CAR-T cells

To substantiate our hypothesis, we engineered CAR-T cells specific to Mesothelin (MSLN) and designated these cells MSLN CAR-T cells (Fig. 2a). Mesothelin, a cell surface glycoprotein, is overexpressed in several malignancies, including lung, pancreatic and ovarian cancer. T cells lacking extracellular expression of a single-stranded variable fragment (scFv) against MSLN were used as controls and were termed MOCK-T cells. Following the transduction of isolated peripheral blood T cells with a lentivirus encoding the CAR construct packaged in a triple plasmid system (Supplementary Fig. 1), we successfully generated CAR-T cells expressing CAR proteins. Notably, the co-expression of CAR protein and green fluorescent protein (GFP) in these cells allowed for an indirect assessment of CAR expression efficiency through the observation of GFP in T cells via fluorescence microscopy. Fluorescence microscopy revealed that both types of lentivirus-transduced T cells exhibited bright green fluorescence, indicating successful CAR protein expression (Fig. 2b). Furthermore, flow cytometry quantification of the CAR protein on the T cell surface revealed a lentiviral transduction efficiency of approximately 64% (Fig. 2c).

To assess the specific cytotoxicity of CAR-T cells against tumor cells, we cocultured them with PC-9 cells and MSLN-overexpressing LLC and B16 cells (designated as LLC-MSLN and B16-MSLN cells). The LLC-MSLN and B16-MSLN cells were generated via lentiviral infection and puromycin screening (Supplementary Figs. 2-3). Inverted fluorescence microscopy revealed a dose-dependent cytotoxic effect of CAR-T cells on PC-9 cells (Fig. 2d). Moreover, the lysis rate of tumor cells by CAR-T cells was quantified by measuring lactate dehydrogenase (LDH) levels in the supernatant. The results indicated superior lysis of PC-9, LLC-MSLN and B16-MSLN cells by MSLN CAR-T cells compared to MOCK-T cells (Figs. 2e, f and Supplementary Fig. 4). Notably, the MSLN CAR-T cells exhibited enhanced secretion of pro-inflammatory cytokines such as tumor necrosis factor-alpha (TNF-α), interleukin-2 (IL-2), interferon-gamma (IFN-γ), and granzyme B in the course of tumor cell eradication relative to that of the MOCK-T cells (Fig. 2g–j and Supplementary Fig. 5).

To further investigate the anti-tumor efficacy of CAR-T cells in vivo, we established murine models of LLC orthotopic lung cancer and B16 lung metastasis. The LLC orthotopic lung cancer model was generated by orthotopic injection of luciferase-tagged LLC-MSLN cells into mice, while the B16 lung metastasis model was established by intravenous injection of luciferase-tagged B16-MSLN cells via the tail vein. The antitumor effects of MSLN CAR-T cells were assessed using an IVIS imaging system following the administration of either MOCK-T cells or MSLN CAR-T cells to tumor-bearing mice. IVIS imaging indicated that MSLN CAR-T cells partially inhibited tumor cell growth in mice, but were unable to eradicate tumor cells completely (Fig. 2k and Supplementary Fig. 6). Survival analysis of the tumor-bearing mice revealed a 100% mortality rate within 35 days in the MSLN CAR-T treatment group (Fig. 2l). Additionally, analysis of the percentage of CAR-T cells in peripheral blood at different time points showed that the proportion of MSLN CAR-T cells peaked on day 7 post-injection and then declined rapidly (Supplementary Fig. 7). These findings underscore that while MSLN CAR-T cells demonstrate potent tumor cytotoxicity in vitro, their antitumor efficacy in vivo is significantly limited.

Preparation and characterization of aPD-L1 NVs@cGAMP

To enhance the antitumor efficacy of CAR-T cells against solid tumors in vivo, we engineered specialized nanovesicles to reverse immunosuppressive tumor microenvironments. Initially, we established a

https://doi.org/10.1038/s41467-024-55751-4

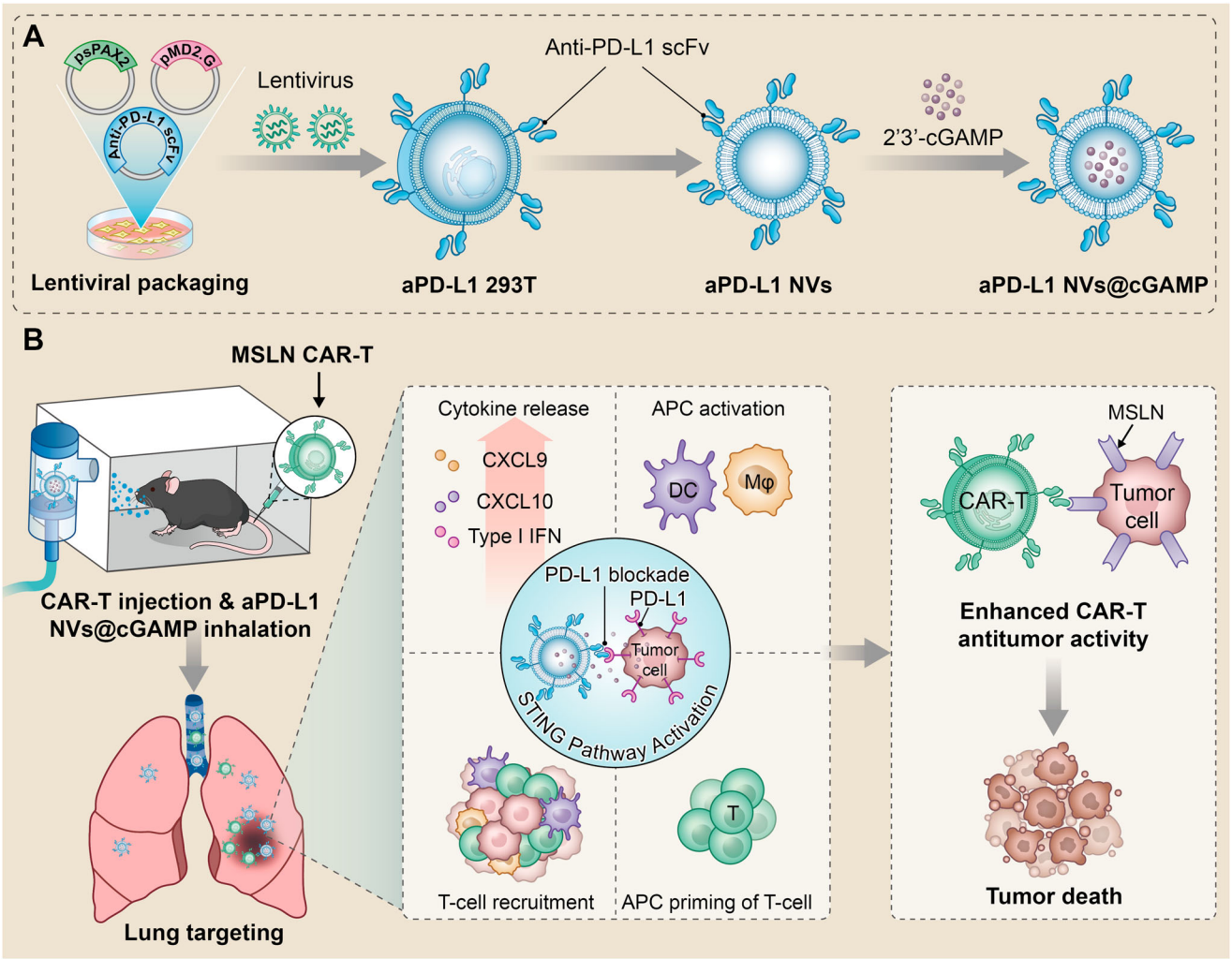

Fig. 1 | Schematic illustration of the ability of aPD-L1 NVs@cGAMP to enhance the antitumor efficacy of CAR-T cells. A Schematic illustration of the preparation process of aPD-L1 NVs@cGAMP. **B** The mechanism by which aPD-L1 NVs@cGAMP enhance the antitumor efficacy of CAR-T cells. The inhaled aPD-L1 NVs@cGAMP rapidly aggregated in lung tissues and delivered STING agonists to cells with high PD-L1 expression in tumor tissues via the PD1/PD-L1 interaction. An internalized STING agonist reversed the suppressive inflammatory tumor microenvironment to a proinflammatory tumor microenvironment by activating the STING pathway, which in turn enhanced the antitumor efficacy of CAR-T cells. In addition, aPD-L1 NVs@cGAMP could effectively prevent CAR-T cell exhaustion by blocking PD-L1. APC: antigen-presenting cell, DC: Dendritic Cells, Mφ: Macrophage.

stable 293 T cell line (aPD-L1 293 T), which was genetically modified to express anti-PD-L1 scFv with GFP-tagged proteins on membranes through lentiviral transduction and puromycin selection. The GFP tag served solely as a fluorescent marker for the anti-PD-L1 scFv in this experiment, and was deleted in subsequent experiments to eliminate its potential functional impact on the scFv. Inverted fluorescence microscopy revealed robust green fluorescence in most lentivirus-transduced 293 T cells, indicating successful expression of the anti-PD-L1 scFv (Fig. 3a). Flow cytometric analysis further confirmed that more than 99% of the 293 T cells post-resistance screening expressed the anti-PD-L1 scFv (Fig. 3b). Importantly, co-incubation experiments demonstrated that the aPD-L1 293 T cells effectively bound recombinant PD-L1 protein, confirming that the anti-PD-L1 scFv expressed on the cell surface retained its antigen-binding capability (Supplementary Fig. 8).

Subsequently, we lysed these modified 293 T cells to extract their membranes, which were then resuspended in PBS. We then produced nanovesicles expressing anti-PD-L1 scFv (aPD-L1 NVs) by subjecting these membranes to serial extrusion through 800 nm and 200 nm polycarbonate membranes. Transmission electron microscopy (TEM) demonstrated that the aPD-L1 NVs were homogenous in structure (Fig. 3c and Supplementary Fig. 9). In addition, the zeta potential of these aPD-L1 NVs was approximately -20 mV (Fig. 3d), which was slightly higher than that of unmodified nanovesicles (Free NVs). The increased zeta potential of aPD-L1 NVs may be attributed to the higher isoelectric point of the anti-PD-L1 scFv, which imparts a slight positive charge to the scFv in neutral solutions[43–45]. The presence of the anti-PD-L1 scFv in these nanovesicles was further confirmed through Western blot analysis (Fig. 3e). To ensure the functional orientation of the scFv, we employed latex bead coupling and subsequent flow cytometric analysis, confirming the outward-facing orientation of the anti-PD-L1 scFv on the aPD-L1 NVs (Fig. 3f).

To evaluate the PD-L1 blocking efficacy of aPD-L1 NVs, we co-incubated these nanovesicles with PD-L1-expressing PC-9 cells. Flow cytometry demonstrated a significant reduction in detectable PD-L1 signals on PC-9 tumor cells pretreated with both aPD-L1 NVs and an anti-PD-L1 antibody compared to those on control cells, confirming effective PD-L1 blockade by aPD-L1 NVs (Fig. 3g). The ability of aPD-L1 NVs to specifically target PD-L1 was further assessed by coincubation with PC-9 cells stably expressing PD-L1 (GFP-PD-L1 PC-9 cells), in which GFP and PD-L1 were tandemly expressed for fluorescent tracking of PD-L1 (Supplementary Fig. 10). Confocal microscopy

https://doi.org/10.1038/s41467-024-55751-4

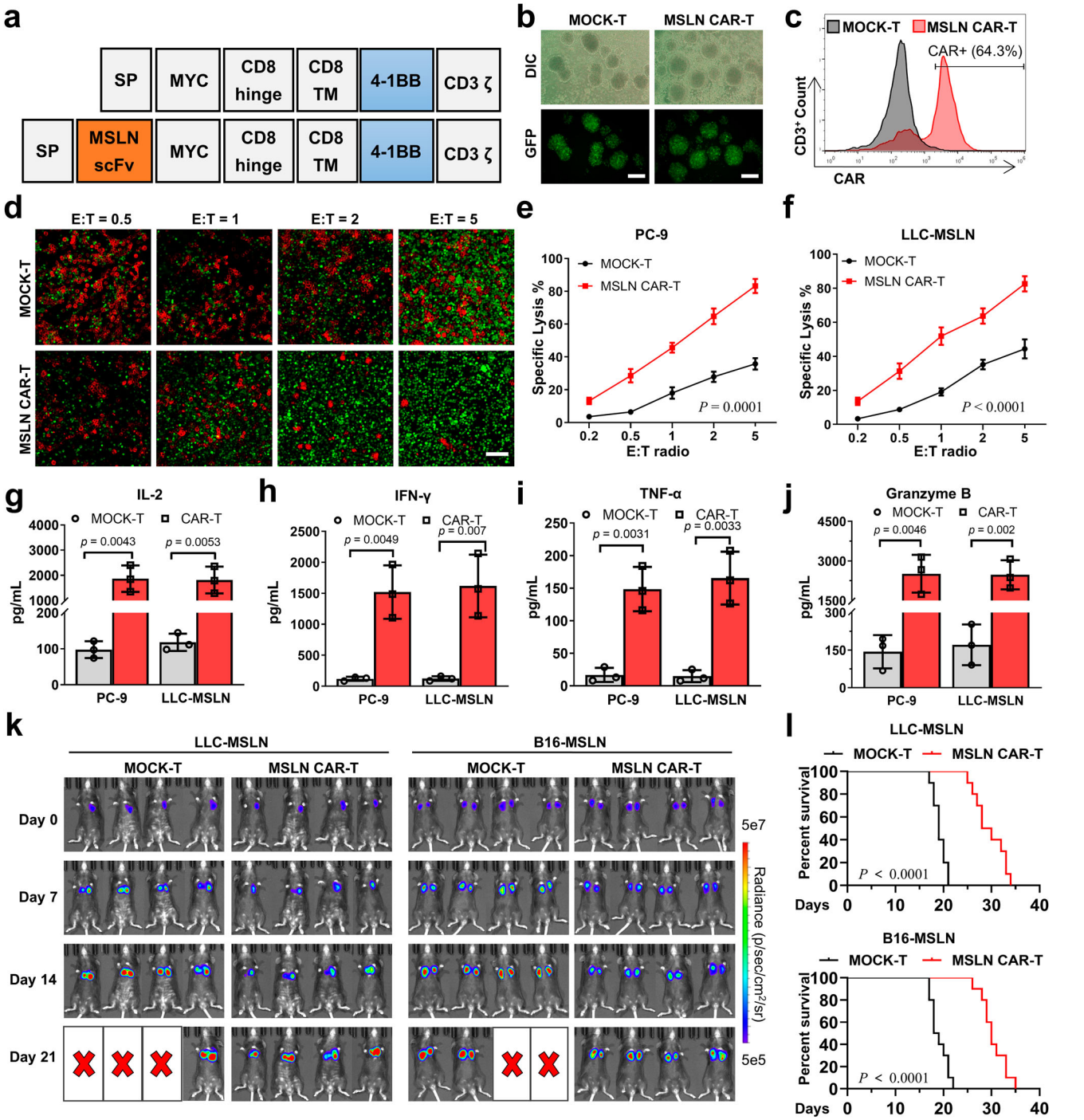

Fig. 2 | Preparation and characterization of MSLN CAR-T cells. a Molecular structures of MOCK-T and MSLN CAR-T cells. **b** Lentiviral transduction efficiency of T cells by inverted fluorescence microscopy. Scale bar: 200 μm. DIC: Differential Interference Contrast, GFP: Green fluorescent protein. **c** Efficiency of CAR protein expression in T cells as determined by flow cytometry. **d** After co-incubation of CAR-T cells (Green) with PC-9 cells (Red) at effector-target ratios (E: T ratios) of 0.5, 1, 2, and 5 for 24 hours, the killing effect of CAR-T cells on PC-9 cells was observed using inverted fluorescence microscopy. Scale bar: 100 μm. **e**, **f** Lysis rates of (**e**) PC-9 cells and (**f**) LLC-MSLN cells induced by CAR-T cells, determined by LDH assay after 24-hour co-incubation at effector-target ratios of 0.2, 0.5, 1, 2, and 5 ($n = 3$ independent experiments). **g**–**j** The levels of cytokines IL-2, IFN-γ, TNF-α and granzyme B in the supernatants were determined by ELISA after co-incubation of CAR-T cells with PC-9 or LLC-MSLN cells ($n = 3$ independent experiments). **k** Antitumor effects of CAR-T cells on LLC-MSLN and B16-MSLN tumor-bearing mice was evaluated using the IVIS system after injection of MOCK-T cells or MSLN CAR-T cells ($n = 4$ mice). **l** Survival curves of LLC-MSLN and B16-MSLN tumor-bearing mice after injection of MOCK-T cells or MSLN CAR-T cells ($n = 10$ mice). All data are presented as the mean ± S.D. The p values were determined by two-way ANOVA with Tukey's post-test for (**e**) and (**f**); by two-tailed Student's t test for (**g**–**j**); and by log rank (Mantel-Cox) test for (**l**). Source data underlying **e**–**j**, **l** are provided as a Source Data file.

revealed greater accumulation of aPD-L1 NVs in GFP-PD-L1 PC-9 cells than in free NVs (Fig. 3h), underscoring the targeted nature of these nanovesicles. Such nanovesicle accumulation on tumor cells was abolished by competitive blockade with anti-PD-L1 antibodies, confirming the specificity of the nanovesicle-tumor interaction mediated by anti-PD-L1 scFvs. Finally, we loaded these nanoparticles with STING agonist (2'3'-cGAMP) to enhance their therapeutic potential (aPD-L1 NVs@cGAMP). This agonist, a non-traditional cyclic

https://doi.org/10.1038/s41467-024-55751-4

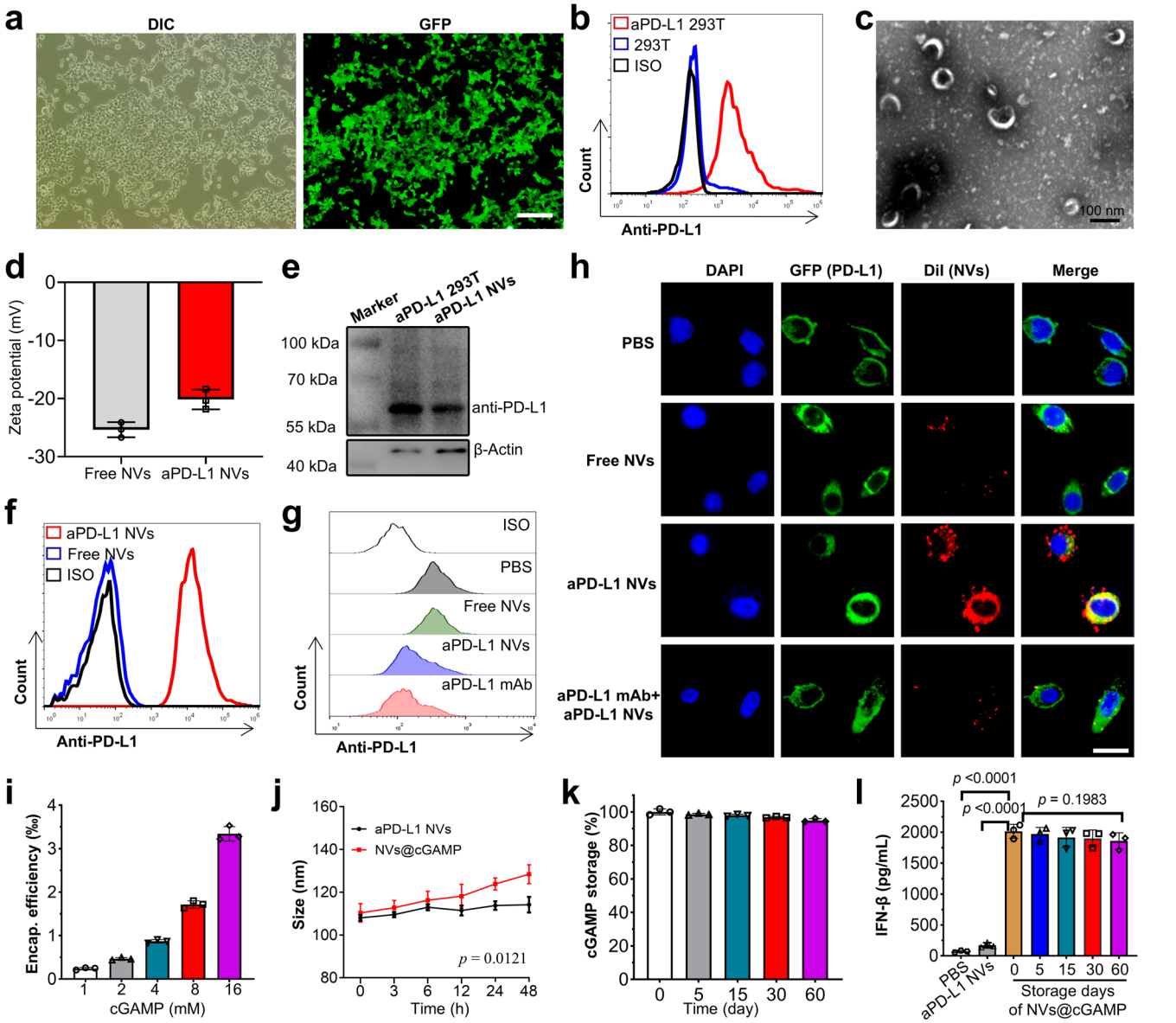

Fig. 3 | Preparation and characterization of aPD-L1 NVs@cGAMP. a 293 T cells stably expressing the anti-PD-L1 scFv were observed via inverted fluorescence microscopy. Scale bar: 200 μm. DIC: Differential Interference Contrast, GFP: Green fluorescent protein. **b** Expression of the anti-PD-L1 scFv on aPD-L1 293 T cells was determined by flow cytometry. **c** The morphology and size of aPD-L1 NVs were detected by transmission electron microscopy. **d** The zeta potential of aPD-L1 NVs was detected by NTA ($n = 3$ independent experiments). e Expression of the anti-PD-L1 scFv protein in aPD-L1 293 T cells and aPD-L1 NVs was detected by Western blotting. Experiment was repeated twice independently with similar results. **f** Expression of the anti-PD-L1 scFv on aPD-L1 NVs was determined by flow cytometry. **g** PD-L1 blockade on the PC-9 cell surface was detected by flow cytometry after coincubation of PC-9 cells with PBS, free NVs, aPD-L1 NVs or aPD-L1 mAb. **h** Confocal microscopy was used to detect the accumulation of DiI-labeled free NVs and aPD-L1 NVs on GFP-PD-L1 PC-9 cells after coincubation. Scale bar: 50 μm. **i** Encapsulation efficiency of aPD-L1 NVs for 2′3′-cGAMP ($n = 3$ independent experiments). **j** Change curve of the particle size of aPD-L1 NVs@cGAMP when stored at room temperature ($n = 3$ independent experiments). **k** Leakage rate of 2′3′-cGAMP from aPD-L1 NVs@cGAMP stored at -80 °C ($n = 3$ independent experiments). **l** Efficiency of aPD-L1 NVs@cGAMP in inducing IFN-β release from DCs after storage at −80 °C for varying durations. DCs treated with PBS and aPD-L1 NVs were used as negative controls ($n = 3$ independent experiments). For **a**, **c** and **h**, experiment was repeated three times independently with similar results. All the data are presented as the mean ± S.D. The p values were determined by two-way ANOVA with Tukey's post-test for (**j**); and by one-way ANOVA with Tukey's post-test for (**l**). Source data underlying **d**, **e**, **i**–**l** are provided as a Source Data file.

dinucleotide, robustly activates diverse STING variants to trigger interferon production. The encapsulation efficiency of 2′3′-cGAMP in the nanovesicles increased in a dose-dependent manner, as depicted in Fig. 3i. The nanovesicles maintained a consistent particle size and dispersion for more than 48 hours, suggesting that the STING agonist had a minimal impact on nanovesicle stability (Fig. 3j). Moreover, these nanovesicles maintained a consistent particle size and exhibited negligible leakage of the STING agonist even after prolonged storage (Fig. 3k). To evaluate whether aPD-L1 NVs@cGAMP could retain their bioactivity over time, we compared the levels of IFN-β secretion and the expression of STING activation–related mRNAs (*IFNB1, IFIT1, IFIT2, and ISG15*) in dendritic cells (DCs) treated with either freshly prepared (day 0) or stored aPD-L1 NVs@cGAMP. As shown in Fig. 3l and Supplementary Fig. 11, DCs treated with aPD-L1 NVs@cGAMP stored at −80 °C for up to two months exhibited IFN-β secretion levels comparable to those treated with freshly prepared nanovesicles, and their STING activation-related mRNA expression was also similar. These results indicate that aPD-L1 NVs@cGAMP

maintain their bioactivity even after long-term storage, which is crucial for potential clinical application.

In vitro bioactivity and biodistribution of aPD-L1 NVs@cGAMP

Following the preparation of aPD-L1 NVs@cGAMP, we investigated its potential to improve the antitumor efficacy of T cells. To this end, LLC-MSLN cells were co-cultured with CAR-T cells at a 2:1 ratio in microtiter plates, and various pharmacological agents were introduced to enhance the anti-tumor activity of the CAR-T cells. Crucially, since dendritic cells (DCs) within the tumor microenvironment often overexpress PD-L1 and are primary target cells for STING agonists[46,47], we included DCs in the experiment to more accurately simulate how aPD-L1 NVs@cGAMP enhances the antitumor capacity of CAR-T cells in vivo. Enzyme-linked immunosorbent assay (ELISA) analyses of the co-culture supernatants revealed that both aPD-L1 NVs@cGAMP and free STING agonists significantly elevated IFN-β secretion. Remarkably, the aPD-L1 NVs@cGAMP required merely 2% of the STING agonist dose used in the free form to induce comparable IFN-β, IL-2, IFN-γ and TNF-α levels, underscoring the efficacy of the nanovesicles in enhancing the potency of the STING agonists (Fig. 4a and Supplementary Fig. 12). In contrast, co-administration of aPD-L1 NVs and free STING agonists did not significantly increase the IFN-β, IL-2, IFN-γ and TNF-α concentration in the supernatant, indicating that synergy between the two is crucial for optimal IFN-β, IL-2, IFN-γ and TNF-α secretion enhancement. This synergistic effect may be attributed to aPD-L1 NVs facilitating the cellular uptake of STING agonists. Typically, STING agonists are hydrophilic and negatively charged, which limits their ability to penetrate cell membranes and results in poor cellular uptake[48,49]. Moreover, free STING agonists are readily degraded by phosphodiesterases on the cell surface and in circulation, leading to a short half-life[50]. In contrast, nanovesicles with lipid bilayer structures can facilitate rapid entry into cells via endocytosis or membrane fusion, thereby improving the intracellular delivery and retention of STING agonists[51]. Studies by Kathleen M. et al. have demonstrated that loading STING agonists into extracellular vesicles increased cellular uptake tenfold compared to free STING agonists[49]. Moreover, aPD-L1 NVs@cGAMP dose-dependently enhanced IFN-β, IL-2, IFN-γ and TNF-α secretion (Fig. 4b and Supplementary Fig. 12). The increased release of proinflammatory factors promoted the proliferation of CAR-T cells, thereby increasing their tumor eradication efficiency. Compared to those in the PBS control group, the aPD-L1 NVs@cGAMP-treated CAR-T cells exhibited a 3-fold increase in proliferation and a 2.3-fold increase in tumor cell eradication (Fig. 4c–f). Notably, even at low concentrations, aPD-L1 NVs@cGAMP significantly stimulated CAR-T cell proliferation and enhanced tumor cell killing in a dose-dependent manner. These results demonstrate the potential of aPD-L1 NVs@cGAMP to improve the antitumor efficacy of CAR-T cells in vitro.

The in vivo biodistribution of aPD-L1 NVs@cGAMP is critical to its therapeutic efficacy. Previous research has suggested that nanovesicles accumulate predominantly in the liver following intravenous administration, limiting their therapeutic impact on extrahepatic tumors[41,52]. To address this issue, we explored the improved lung-specific distribution of aPD-L1 NVs@cGAMP via nebulized administration, aiming to enhance its efficacy in modulating lung tumor microenvironments. Post-administration of DiR-labeled aPD-L1 NVs@cGAMP via intravenous injection or inhalation, we assessed the nanovesicles' biodistribution across various mouse organs using IVIS imaging. The biofluorescence intensity in the lung tissue of the inhalation group was 5.5 times greater than that observed in the intravenous group, indicating a significant enhancement in lung bioavailability via nebulization (Fig. 4g). In addition, confocal microscopy analysis of immunofluorescence-stained lung tissue sections confirmed these findings, showing greater accumulation of DiI-labeled aPD-L1 NVs@cGAMP in the lungs following nebulized administration than after intravenous administration (Fig. 4h). IVIS imaging also revealed dose-dependent accumulation of aPD-L1 NVs@cGAMP in the lungs (Fig. 4i). To optimize dosing intervals, we further evaluated the time-dependent distribution of these nanovesicles in vivo. Notably, the lung accumulation of aPD-L1 NVs@cGAMP after inhalation decreased progressively from 6 to 48 hours (Fig. 4j). Interestingly, flow cytometry analyses indicated that the nanovesicles were taken up after inhalation not only by tumor cells with high PD-L1 expression, but also by DCs and macrophages (Fig. 4k). This observation is consistent with studies showing that DCs in the tumor microenvironment often overexpress PD-L1, which affects T cell activity. Finally, we analyzed STING agonist levels in various organs following nebulized delivery of aPD-L1 NVs@cGAMP. The results indicated a predominant aggregation of STING agonists in the lung (Fig. 4l), suggesting that nebulized delivery could effectively increase the STING agonist concentration in the lung, thereby altering the tumor microenvironment and potentially mitigating cytokine storm.

Remodeling of the tumor microenvironment and inhibition of tumor growth by aPD-L1 NVs@cGAMP

To evaluate the capacity of aPD-L1 NVs@cGAMP to remodel immunosuppressive tumor microenvironments in vivo, we established a murine model of LLC orthotopic lung cancer by orthotopic injection of luciferase-tagged LLC-MSLN cells into the lungs of mice. After nebulized administration to tumor-bearing mice, we analyzed the mRNA expression levels of key inflammatory markers within the lung tumors by qPCR. Remarkably, despite encapsulating 50-fold less STING agonist than free cGAMP controls, aPD-L1 NVs@cGAMP elicited 2-fold, 2.4-fold, and 2.9-fold greater upregulation of IFN-β, CXCL9, and CXCL10, respectively (Fig. 5a). This increased expression of CXCL9 and CXCL10 is critical because it is likely to facilitate the recruitment of $CD8^+$ T cells into tumor tissue, thereby enhancing the antitumor immune response. In contrast, aPD-L1 NVs did not significantly influence the mRNA expression levels of these proinflammatory factors. Furthermore, both aPD-L1 NVs@cGAMP and free STING agonist treatment significantly upregulated PD-L1 mRNA expression in tumor tissues (Fig. 5a), which might contribute to T cell exhaustion and subsequent immune evasion by tumor cells. However, it is important to note that although the high expression of PD-L1 induced by STING agonists increases the risk of T cell exhaustion, they overall still play an antitumor role. Previous studies have demonstrated that STING agonists not only induce the production of cytokines (such as IFN-β, CXCL9, and CXCL10) beneficial for T cell activation and proliferation but may also enhance the antitumor capacity of T cells by promoting the maturation of DCs and directly acting on tumor cells[53–55]. Therefore, blocking the high PD-L1 expression induced by STING agonists would be advantageous to further amplify these antitumor effects. Fortunately, flow cytometry results indicated that aPD-L1 NVs@cGAMP effectively blocked PD-L1 overexpression on tumor cell surfaces (Supplementary Fig. 13). Next, we further investigated alterations in the T cell populations within the tumor tissues using flow cytometry. The results revealed a significantly greater $CD8^+/CD4^+$ T cell ratio in the aPD-L1 NVs@cGAMP group than in the cGAMP, aPD-L1 NVs and PBS groups, indicating an increase in $CD8^+$ T-cell infiltration into tumor sites (Fig. 5b). Additionally, the proportion of Tregs and MDSCs in the aPD-L1 NVs@cGAMP group was lower than in other treatment groups (Fig. 5c, d), suggesting a reduction in the accumulation of immunosuppressive cells within the tumor environment. Compared to the free cGAMP group, the exhaustion markers (PD-1, TIM-3, LAG-3, and TIGIT) on T cells were decreased in the aPD-L1 NVs@cGAMP group (Fig. 5e, f). This finding indicates that the anti-PD-L1 scFv on the surface of aPD-L1 NVs@cGAMP may help alleviate T-cell exhaustion. Furthermore, T cells in the aPD-L1 NVs@cGAMP group expressed higher levels of CD25 (Supplementary Fig. 14), suggesting that T cells in this group were more activated. In addition, treatment with aPD-L1 NVs@cGAMP upregulated T helper 1

https://doi.org/10.1038/s41467-024-55751-4

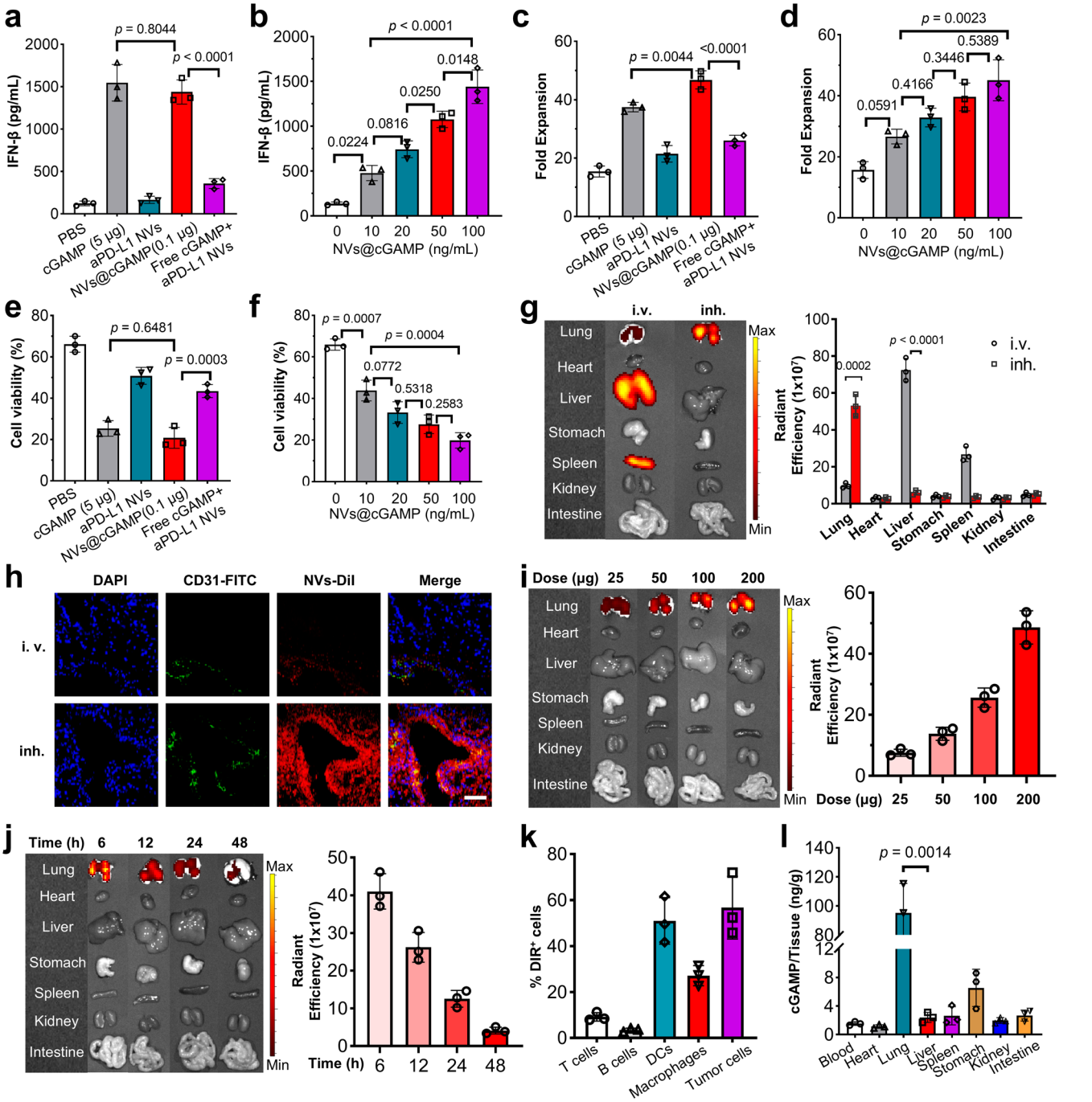

Fig. 4 | In vitro bioactivity and biodistribution of aPD-L1 NVs@cGAMP. a, **b** IFN-β levels in supernatants were measured after 12 h of adding various agents (**a**) or different doses of aPD-L1 NVs@cGAMP (**b**) into a co-incubation system of CAR-T cells, DCs and LLC-MSLN cells (n = 3 independent experiments). **c**, **d** Fold expansion of CAR-T cells was examined after 5 days of adding various agents (**c**) or increasing doses of aPD-L1 NVs@cGAMP (**d**) to CAR-T cells, DCs and LLC-MSLN cells co-incubation ($n = 3$ independent experiments). **e**, **f** Tumor cell lysing capacity of CAR-T cells was evaluated after 12 h of adding different reagents (**e**) or graded doses of aPD-L1 NVs@cGAMP (**f**) to the co-incubation system of CAR-T cells, DCs and LLC-MSLN cells ($n = 3$ independent experiments). **g** Six hours after intravenous (i.v.) or inhaled (inh.) administration, the biodistribution of Dil-labeled aPD-L1 NVs@cGAMP was visualized by IVIS ($n = 3$ mice). **h** Immunofluorescence staining images of lung tissues 6 h from mice injected intravenously or inhaled with Dil-labeled aPD-L1 NVs@cGAMP. Scale bar: 100 μm. Experiment was repeated three times independently with similar results. **i**, **j** The biodistribution of Dil-labeled aPD-L1 NVs@cGAMP within major organs was further analyzed at 6 h after inhalation of varying doses (**i**) or at different time points (**j**) ($n = 3$ mice). **k** Uptake of Dil-labeled aPD-L1 NVs@cGAMP by various cells in tumor microenvironment was analyzed by flow cytometry 6 h after inhalation ($n = 3$ mice). **l** 2′3′-cGAMP accumulation in different organs 6 h after inhalation of aPD-L1 NVs@cGAMP ($n = 3$ mice). All data are presented as the mean ± S.D. The p values were determined by one-way ANOVA with Tukey's post-test for (**a**–**f**); and by two-tailed Student's t test for (**g**) and (**l**). Source data underlying **a**–**g**, **i**–**l** are provided as a Source Data file.

(Th1) and Th17 cells in the TME while downregulating Th2 cells (Fig. 5g, h). The increased Th1/Th2 ratio may be directly associated with PD-L1 blockade, elevated IFN-γ levels, and decreased TGF-β levels induced by aPD-L1 NVs@cGAMP[56,57]. PD-L1 blockade and increased IFN-γ promote the differentiation of naive $CD4^+$ T cells into Th1 cells, whereas reduced TGF-β levels inhibit the differentiation into Th2 cells. Furthermore, the upregulation of Th17 cells may be directly associated with the increased IL-6 levels and the pro-inflammatory microenvironment

https://doi.org/10.1038/s41467-024-55751-4

induced by aPD-L1 NVs@cGAMP[58,59]. The shift toward a Th1/Th17 phenotype is beneficial, as Th1 cells promote cell-mediated immunity and are crucial for effective antitumor responses, while Th17 cells can enhance immune surveillance. Importantly, the proportion of central memory T cells (T_{CM}) and effector memory T cells (T_{EM}) were significantly higher in the aPD-L1 NVs@cGAMP group compared to other groups (Fig. 5i, j), suggesting that aPD-L1 NVs@cGAMP treatment may enhance the body's long-term antitumor immunity by promoting T-cell memory formation.

Given the ubiquitous expression of STING proteins, overstimulation by STING agonists could lead to systemic immune hyperactivation. Consequently, we measured cytokine levels (IL-6, TNF-α, IFN-γ, and IFN-β) in both serum and lung tissues using ELISA. Consistent with the qPCR results, the levels of these proinflammatory

Fig. 5 | Remodeling of the tumor microenvironment and inhibition of tumor growth by aPD-L1 NVs@cGAMP. a Changes in the gene expression levels of IFN-β, CXCL9, CXCL10, and PD-L1 in tumor tissues of LLC-MSLN tumor-bearing mice after inhalation of the different agents ($n = 4$ mice). (b-d) Representative flow cytometry plots and statistical analysis of (**b**) $CD8^+$ T cells and $CD4^+$ T cells, (**c**) Treg cells and (**d**) MDSCs within the TME across various treatment groups ($n = 4$ mice). **e**, **f** Representative flow cytometry plots and statistical analysis of T cell exhaustion markers (PD-1, TIM-3, LAG-3, TIGIT) on T cells across different treatment groups by flow cytometry ($n = 4$ mice). **g**, **h** Representative flow cytometry plots and statistical analysis of Th1, Th2, and Th17 cells within the TME across different treatment groups ($n = 4$ mice). **i**, **j** Representative flow cytometry plots and statistical analysis of naïve T cells, central memory T cells (T_{CM}), and effector memory T cells (T_{EM}) within the TME across different treatment groups ($n = 4$ mice). **k** Concentrations of IL-6, TNF-α, IFN-γ and IFN-β in the lung tissue and serum of mice after inhalation of different agents ($n = 4$ mice). **l** Bioluminescence measured by an IVIS system for assessment of tumor growth after administration of different agents to tumor-bearing mice. **m** Survival curves of tumor-bearing mice treated with different agents ($n = 10$ mice). All data are presented as the mean ± S.D. The p values were determined by one-way ANOVA with Tukey's post-test for (**a**–**d**), (**f**), (**h**–**i**) and (**j**); by two-tailed Student's t test for (**k**); and by log rank (Mantel-Cox) test for (**m**). Source data underlying **a**–**d**, **f**, **h**, **i**, **k**, **m** are provided as a Source Data file.

cytokines in lung tissue were greater in the aPD-L1 NVs@cGAMP group than in the free STING agonist group, even though the concentration of the STING agonist in the aPD-L1 NVs@cGAMP group was significantly lower (Fig. 5k). Crucially, the serum cytokine levels were significantly lower in the aPD-L1 NVs@cGAMP group than in the free STING agonist group. This finding underscores the potential of aPD-L1 NVs@cGAMP to achieve local inflammation without triggering systemic inflammatory responses, thereby reducing the likelihood of adverse clinical events such as cytokine storms.

Finally, to assess the antitumor efficacy of aPD-L1 NVs@cGAMP in vivo, we constructed murine LLC orthotopic lung cancer and B16 lung metastasis models using luciferase-labeled LLC-MSLN cells and B16-MSLN cells, respectively. Tumor progression was evaluated by the IVIS system on the 7th and 14th days following treatment administration on days 0 and 3. The results revealed that tumor growth inhibition by aPD-L1 NVs@cGAMP was significantly superior to that observed with high doses of cGAMP and aPD-L1 NVs (Fig. 5i and Supplementary Fig. 15). In addition, aPD-L1 NVs@cGAMP caused more damage to tumor tissue as demonstrated by TUNEL staining of tumor tissue sections (Supplementary Fig. 16). Survival curve analysis further supported these findings, showing a significant increase in survival for mice treated with aPD-L1 NVs@cGAMP (Fig. 5m). Collectively, these results validate the capacity of aPD-L1 NVs@cGAMP to reverse immunosuppressive tumor microenvironments and inhibit metastatic growth in vivo.

Enhancement of the antitumor capacity of CAR-T cells by aPD-L1 NVs@cGAMP

Having confirmed the ability of aPD-L1 NVs@cGAMP to remodel the immunosuppressive tumor microenvironment, we next investigated whether this remodeling could enhance CAR-T cell efficacy against metastatic lung cancer in vivo. We established LLC-MSLN orthotopic lung cancer and B16-MSLN lung metastasis mouse models and treated the tumor-bearing mice with different regimens (Fig. 6a). The IVIS imaging system results showed universal suppression of tumor progression in all treated groups compared to the control (PBS-treated) group (Fig. 6b, c). Notably, the group treated with a combination of CAR-T cells and inhaled aPD-L1 NVs@cGAMP—referred to as the CAR-T +NVs@cGAMP (inh.) group—exhibited negligible fluorescence signals in both tumor models, indicating almost complete tumor eradication. In contrast, monotherapies with either CAR-T cells or aPD-L1 NVs@cGAMP achieved only partial tumor growth inhibition. Interestingly, the group treated with CAR-T cells and intravenously administered aPD-L1 NVs@cGAMP did not effectively inhibit tumor progression, suggesting that localized aerosol inhalation delivery of aPD-L1 NVs@cGAMP directly to the lung tissues is crucial for its optimal anti-tumor efficacy. After 14 days of treatment, the mice were sacrificed, and their lung tissues were collected and sectioned for pathological examination. Histopathology analysis revealed that mice in the CAR-T+NVs@cGAMP (inh.) group had minimal pathological alterations in lung tissues across both tumor models, whereas significant pathological changes persisted in the lungs of mice treated with either CAR-T cells alone or NVs@cGAMP alone (Fig. 6d). Particularly in the B16-MSLN metastatic lung cancer model, obvious lung metastases were observed in the lung tissues of mice treated with CAR-T cells or aPD-L1 NVs@cGAMP alone, while lung metastases were minimal in the CAR-T+NVs@cGAMP (inh.) group (Supplementary Fig. 17). Throughout the observation period, mice in the PBS group experienced significant weight loss due to tumor-induced cachexia, while those in the CAR-T+NVs@cGAMP group experienced gradual weight gain (Fig. 6e). Crucially, survival analysis revealed that mice in the CAR-T+NVs@cGAMP group achieved 100% survival on day 50 posttreatment, in stark contrast to the complete mortality observed in the other groups (Fig. 6f). This finding underscores the potential of CAR-T+NVs@cGAMP for significantly enhancing the survival of tumor-bearing mice.

Next, we evaluated the safety of combined therapy with CAR-T cells and aPD-L1 NVs@cGAMP in healthy C57BL/6 mice. After the administration of PBS or the combined treatment to the mice, blood samples were collected for biochemical analysis. Aspartate aminotransferase (AST), alanine aminotransferase (ALP) and alanine aminotransferase (ALT) are indicators of liver function in mice, while blood urea nitrogen (BUN) and creatinine (CR) are indicators of kidney function in mice. Serum proteins and liposomes were also analyzed. The results showed that the levels of these biochemical indicators in the combined treatment group were not significantly different from those in the PBS group (Fig. 6g and Supplementary Fig. 18). In addition, histomorphological changes in the major organs of the mice after combined treatment were also observed. Hematoxylin and eosin (H&E) staining revealed no significant pathological morphological changes in the major organs of the mice after the combined treatment (Fig. 6h). These results suggest that combined treatment with CAR-T cells and aPD-L1 NVs@cGAMP has a favorable safety profile.

\Changes in the tumor microenvironment after CAR-T + NVs@cGAMP treatment

To elucidate the underlying mechanisms driving the potent antitumor efficacy of CAR-T+NVs@cGAMP, we investigated the proliferative capacity and cellular activity of CAR-T cells and the resulting changes in the tumor microenvironment. To track the proliferation of CAR-T cells in a live setting, we generated MSLN CAR-T cells expressing luciferase. IVIS analysis revealed that CAR-T cells in the CAR-T +NVs@cGAMP (inh.) group exhibited a significantly increased proliferation rate compared with those receiving CAR-T cell therapy alone, suggesting that aPD-L1 NVs@cGAMP significantly enhanced CAR-T cell proliferation in vivo (Fig. 7a). Analysis of the percentages of CAR-T cells in peripheral blood at different time points demonstrated that in the CAR-T + NVs@cGAMP (inh.) group, CAR-T cells accounted for up to 13.8% of T cells 14 days post-injection, followed by a gradual decline. In contrast, in the CAR-T group, the percentage of CAR-T cells peaked at only 3% after 7 days post-injection and then rapidly decreased (Supplementary Fig. 19). This indicates that NVs@cGAMP inhalation significantly prolongs the persistence of CAR-T cells in vivo. Furthermore, confocal microscopy was employed to detect CAR-T cells in the lungs and spleens of mice from different treatment groups. The results demonstrated that the density of CAR-T cells in the lung tumor tissues and spleens of the CAR-T + NVs@cGAMP (inh.) group was substantially

https://doi.org/10.1038/s41467-024-55751-4

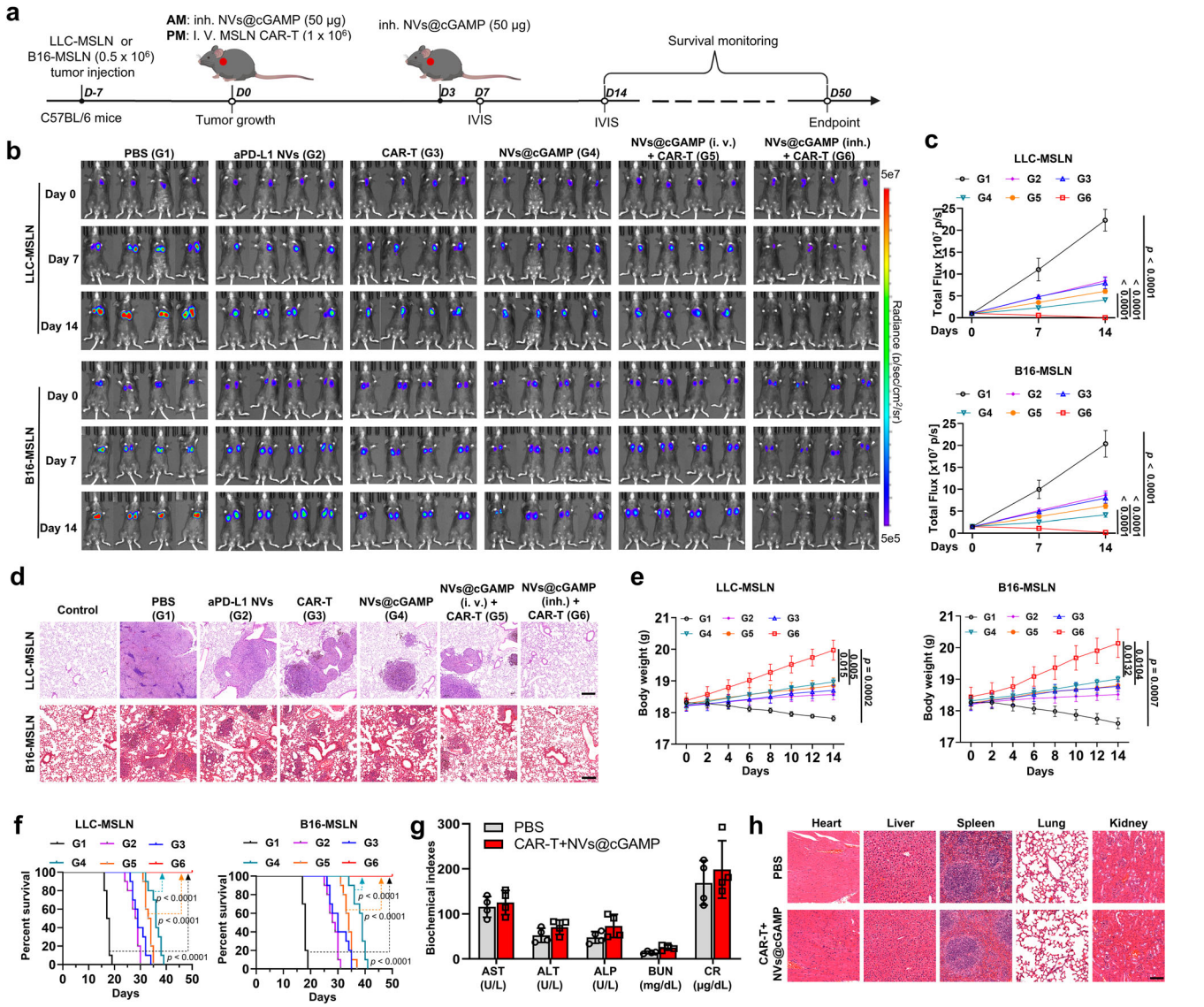

Fig. 6 | Enhancement of the antitumor capacity of CAR-T cells by aPD-L1 NVs@cGAMP. a Schematic illustration of aPD-L1 NVs@cGAMP augmenting CAR-T cell anti-tumor efficacy. i.v.: Intravenous, inh.: Inhalation, IVIS: In vivo imaging system, AM: Ante meridiem, PM: Post meridiem. **b**, **c** Bioluminescence was measured by the IVIS system to evaluate tumor growth in the different treatment groups, and the bioluminescence intensity was statistically analyzed ($n = 4$ mice). **d** Representative images of H&E-stained sections from LLC-MSLN and B16-MSLN tumor-bearing mice in various treatment groups ($n = 4$ mice). **e** Body weight change curves of mice treated with different agents in both tumor models ($n = 4$ mice). **f** Survival curves of mice treated with different agents in both tumor models ($n = 10$ mice). **g** Serum biochemical indices of mice receiving PBS or combined treatment with CAR-T cells and aPD-L1 NVs@cGAMP ($n = 4$ mice). **h** Representative lung images and H&E-stained sections of mice receiving PBS or combined treatment with CAR-T cells and aPD-L1 NVs@cGAMP. Scale bar: 100 μm. All the data are presented as the mean ± S.D. The p values were determined by two-way ANOVA with Tukey's post-test for (**c**) and (**e**); and by log rank (Mantel-Cox) test for (**f**). Source data underlying **c**, **e**–**g** are provided as a Source Data file.

higher than that in the CAR-T and CAR-T+ NVs@cGAMP (i.v.) groups (Supplementary Fig. 20). Quantitative PCR (qPCR) analysis for DNA quantification of CAR-T cells in tumor tissues further confirmed these findings, revealing greater infiltration of CAR-T cells into the tumor milieu in the CAR-T+NVs@cGAMP group (Supplementary Fig. 21). Previous studies have indicated that STING agonists can improve T cell infiltration by activating the STING pathway, counteracting endothelial dysfunction[53]. However, STING agonists may also induce high PD-L1 expression on tumor vasculature, promoting CAR-T cell exhaustion[55]. Therefore, we examined PD-L1 expression on lung tumor vasculature using confocal microscopy. The results showed that the free cGAMP treatment group induced high expression of PD-L1 on tumor vasculature, whereas only minimal PD-L1 expression was detected in the CAR-T + NVs@cGAMP (inh.) group (Supplementary Fig. 22). This suggests that the anti-PD-L1 scFv on the surface of NVs@cGAMP effectively blocked the PD-L1 induced by the STING agonist.

To elucidate the impact of CAR-T+NVs@cGAMP (inh.) on the tumor microenvironment, we analyzed alterations in immune cell populations within the tumor milieu using flow cytometry. Flow cytometry results revealed that the ratio of $CD8^+/CD4^+$ T cells in the CAR-T + NVs@cGAMP (inh.) group was significantly higher than in other treatment groups (Fig. 7b). An elevated $CD8^+$ T cell population is advantageous for antitumor immune responses, as $CD8^+$ cytotoxic T lymphocytes are key effectors in tumor cell killing. Given that granzyme B is a key cytotoxic effector in T cell-mediated tumor cell lysis, we quantified the frequency of granzyme B-expressing $CD8^+$ T cells in tumor tissues. Compared to the groups treated with CAR-T cells or aPD-L1 NVs@cGAMP alone, the CAR-T+NVs@cGAMP (inh.) group

https://doi.org/10.1038/s41467-024-55751-4

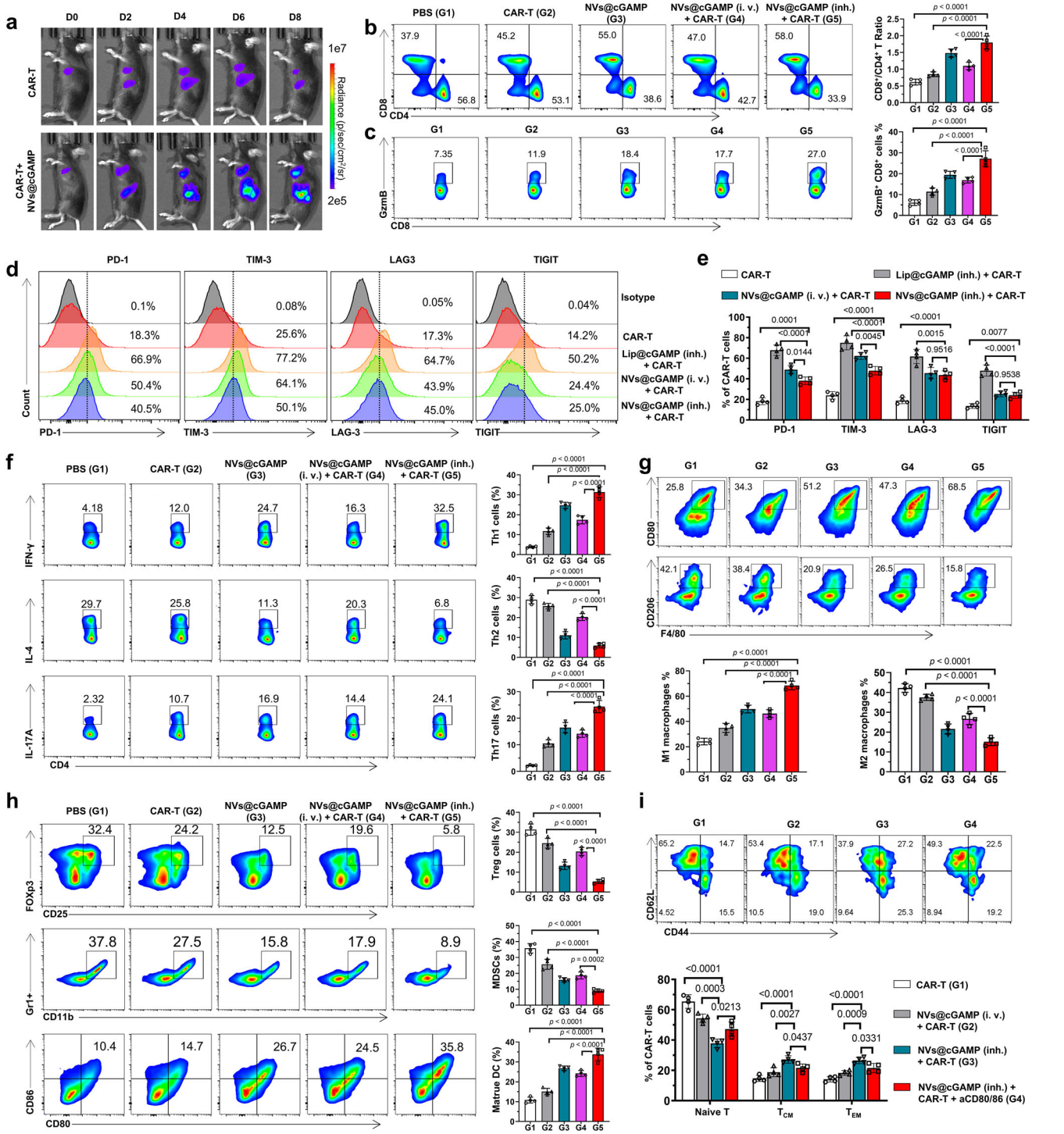

Fig. 7 | Changes in the tumor microenvironment after CAR-T + NVs@cGAMP treatment. a To assess the proliferation of CAR-T cells in different treatment groups, bioluminescence intensity was measured by IVIS at different time points after the injection of CAR-T cells expressing luciferase. **b**, **c** Representative flow cytometry plots and statistical analysis of (b) $CD8^+$ T cells and $CD4^+$ T cells and (**c**) infiltrating granzyme B-expressing $CD8^+$ T cells within the TME across various treatment groups ($n = 4$ mice). **d**, **e** Representative flow cytometry plots and statistical analysis of T cell exhaustion markers (PD-1, TIM-3, LAG-3, TIGIT) on CAR-T within the TME across various treatment groups ($n = 4$ mice). **f** Representative flow cytometry plots and statistical analysis of Th1, Th2 and Th17 within the TME across various treatment groups ($n = 4$ mice). **g** Representative flow cytometry plots and statistical analysis of M1-type and M2-type macrophages within the TME across various treatment groups ($n = 4$ mice). **h** Representative flow cytometry plots and statistical analysis of Tregs, MDSCs and mature DCs within the TME across various treatment groups ($n = 4$ mice). **i** Representative flow cytometry plots and statistical analysis of naïve T cells, central memory T cells (T_{CM}), and effector memory T cells (T_{EM}) within the CAR-T cell population in the TME across different treatment groups ($n = 4$ mice). All the data are expressed as mean ± S.D. The p values were determined by one-way ANOVA with Tukey's post-test for (**b**, **c**) and (**e**–**i**). Source data underlying **b**, **c**, **e**–**i** are provided as a Source Data file.

https://doi.org/10.1038/s41467-024-55751-4

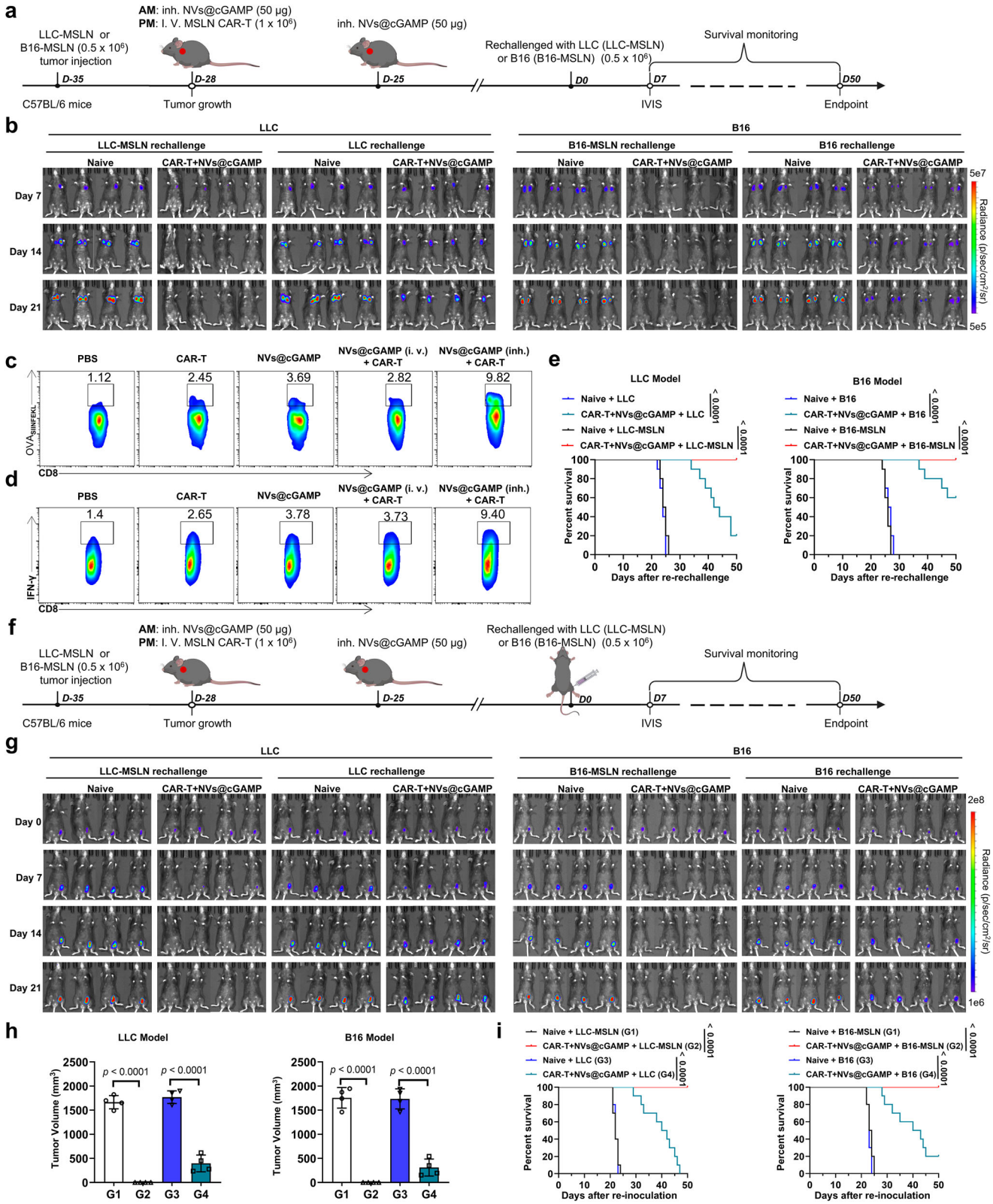

exhibited increased infiltration of granzyme B-expressing $CD8^+$ T cells into the tumor tissue (Fig. 7c). Additionally, CAR-T+NVs@cGAMP (inh.) treatment induced higher levels of CD69 expression in T cells (Supplementary Fig. 23), signifying greater T cell activation. Activation of CAR-T cells by NVs@cGAMP inevitably induces the expression of T cell exhaustion markers. However, it is noteworthy that compared to inhalation of liposomes loaded with STING agonists, inhalation of NVs@cGAMP induced lower expression levels of CAR-T cell exhaustion markers (Fig. 7d, e). This suggests that NVs@cGAMP may minimize exhaustion while promoting activation.

Moreover, the CAR-T + NVs@cGAMP (inh.) group upregulated Th1 and Th17 cells in the TME while downregulating Th2 cells (Fig. 7f). Th1 and Th17 cells are associated with proinflammatory and antitumor responses, whereas Th2 cells are linked to anti-inflammatory and

Fig. 8 | Inhibition of tumor recurrence by combined therapy with CAR-T cells and NVs@cGAMP. a Schematic illustration of the experimental design for evaluating anti-recurrence efficacy of MSLN CAR-T cells combined with NVs@cGAMP in LLC-MSLN and B16-MSLN tumor-bearing mice. **b** Both naive mice and those cured by combination therapy were re-challenged with either parental tumor cells (LLC or B16) or their MSLN-expressing counterparts (LLC-MSLN or B16-MSLN). Bioluminescence intensity was measured using the IVIS system to assess tumor recurrence ($n = 4$ mice). **c** In LLC-MSLN-OVA tumor-bearing mice, $OVA_{(SIINFEKL)}$-specific $CD8^+$ T cells in the spleen were quantified by flow cytometry after various treatments. **d** Following OVA peptide stimulation, the frequency of IFN-γ–producing $CD8^+$ T cells was evaluated by flow cytometry. **e** Survival curves were generated for naive mice and cured mice after intravenous re-inoculation with either parental (LLC or B16) or MSLN-expressing tumor cells (LLC-MSLN or B16-MSLN) in both models ($n = 10$ mice). **f** A schematic illustrates the evaluation of resistance to ectopic tumor recurrence. **g** In both models, naive mice and cured mice were subcutaneously re-inoculated in the groin with either parental or MSLN-expressing tumor cells, and recurrence was tracked by IVIS imaging ($n = 4$ mice). **h** Tumor volumes were measured following subcutaneous rechallenge with LLC or LLC-MSLN cells (LLC model) and B16 or B16-MSLN cells (B16 model) ($n = 4$ mice). Data represent the mean ± SD. **i** Survival curves of naive mice and mice cured by combined therapy after subcutaneous inoculation of either the parental tumor cells (LLC or B16) or their MSLN-expressing counterparts (LLC-MSLN or B16-MSLN) in both tumor models ($n = 10$ mice). i.v.: Intravenous, inh.: Inhalation, IVIS: In vivo imaging system, AM: Ante meridiem, PM: Post meridiem. The p values were determined by one-way ANOVA with Tukey's post-test for (**h**); and by log rank (Mantel-Cox) test for (**e**) and (**i**). Source data underlying e, **h**, **i** are provided as a Source Data file.

tumor-promoting activities[60]. This shift in the Th1/Th2 balance is conducive to enhancing the antitumor capacity of CAR-T cells. Considering the crucial roles of macrophages in immune regulation, we investigated their proportions in tumor tissues. Flow cytometry revealed that the CAR-T+NVs@cGAMP and aPD-L1 NVs@cGAMP groups had a significant increase in M1-type (pro-inflammatory) macrophages and a decrease in M2-type (anti-inflammatory) macrophages compared to the CAR-T cell group (Fig. 7g). This shift in the M1/M2 ratio contributes to a more pro-inflammatory and antitumor microenvironment. Furthermore, we performed immunohistochemical analysis to assess the expression of inducible nitric oxide synthase (iNOS) and cyclooxygenase-2 (COX-2) in tumor tissues (Supplementary Fig. 24). iNOS is predominantly expressed by M1 macrophages and plays a critical role in antitumor immunity by producing nitric oxide (NO). Conversely, high expression of COX-2 can promote angiogenesis by increasing prostaglandin levels, thereby enhancing the invasiveness of tumor cells. Immunohistochemical results showed that the combination of CAR-T and NVs@cGAMP (inh.) effectively increased the expression of iNOS in tumor tissues while reducing the expression of COX-2.

In addition, we examined the populations of regulatory T cells (Tregs) and myeloid-derived suppressor cells (MDSCs) within the tumor tissue. These cell types are known to inhibit T cell-mediated antitumor responses and promote immune evasion of tumor cells by secreting anti-inflammatory cytokines and angiogenic factors. Flow cytometry analyses revealed that CAR-T+NVs@cGAMP (inh.) significantly reduced the proportions of Tregs and MDSCs in the tumor microenvironment (Fig. 7h), indicating that this treatment effectively inhibited the accumulation of immunosuppressive cells at tumor sites. Furthermore, the ability of CAR-T+NVs@cGAMP (inh.) to promote DC maturation in tumor tissues was evaluated by assessing the expression of CD80 and CD86 on DC surfaces. The flow cytometry results indicated that CAR-T+NVs@cGAMP (inh.) and aPD-L1 NVs@cGAMP were more efficient at inducing DC maturation than CAR-T cells alone (Fig. 7h). To assess the effect of upregulated CD80 and CD86 on mature DCs in activating CAR-T cells and enhancing their long-term antitumor function, we used anti-CD80 and anti-CD86 antibodies to block these molecules on the surface of DCs. The results showed that, compared with the CAR-T + NVs@cGAMP (inh.) treatment group without antibody blockade, the expression of CD69 on CAR-T cells in the group receiving both anti-CD80 and anti-CD86 antibodies was significantly reduced (Supplementary Fig. 25), indicating that the blockade of CD80 and CD86 weakened CAR-T cell activation. Additionally, the proportions of central memory (T_{CM}) and effector memory (T_{EM}) CAR-T cells were significantly lower in the antibody-blocked group (Fig. 7i), suggesting adverse effects on immune memory formation and long-term antitumor capacity. These results underscore the importance of NVs@cGAMP-induced mature DCs in enhancing CAR-T cell activation and sustaining their antitumor activity. Importantly, the proportions of T_{CM} and T_{EM} among CAR-T cells in the CAR-T + NVs@cGAMP (inh.) group were significantly higher than those in the CAR-T group and the CAR-T + NVs@cGAMP (i.v.) group (Fig. 7i), indicating that NVs@cGAMP (inh.) may help promote the long-term memory immunity of CAR-T cells.

Finally, we investigated the modulation of cytokine levels within the tumor tissue, as these soluble factors play a key role in orchestrating the immune response. Using ELISA, we observed that CAR-T +NVs@cGAMP significantly increased the levels of IL-1β, IL-6, IL-7, IL-12, IL-15, and TGF-α in the tumor milieu (Supplementary Fig. 26). These cytokines are known to enhance the activity of immune cells within tumors and promote the formation of long-lasting T-cell memory. Conversely, the levels of the immunosuppressive cytokine IL-10 and TGF-β (Supplementary Fig. 26), which promotes tumor cell escape from immune surveillance, were significantly reduced after CAR-T+NVs@cGAMP treatment. Taken together, these results demonstrate that aPD-L1 NVs@cGAMP can effectively reverse the immunosuppressive tumor microenvironment, rendering it proinflammatory and conducive to CAR-T cell proliferation and function.

Inhibition of tumor recurrence by combined therapy with CAR-T cells and aPD-L1 NVs@cGAMP

The issue of tumor relapse after initial clinical remission poses a formidable challenge to the efficacy of CAR-T cell therapies. To address this issue, we used murine models of tumor relapse to evaluate the ability of CAR-T+NVs@cGAMP to prevent tumor relapse. After tumor eradication with CAR-T +NVs@cGAMP, the cured mice were rechallenged to simulate tumor relapse. Specifically, LLC (or LLC-MSLN) cells and B16 (or B16-MSLN) cells were reintroduced into these mice via orthotopic and tail vein injections, respectively (Fig. 8a). As a control, naive mice without any treatment received the same treatment. IVIS analysis revealed that mice treated with CAR-T + NVs@cGAMP showed no detectable fluorescence signals upon re-injection with LLC-MSLN or B16-MSLN cells, indicating effective resistance against tumor cells harboring identical antigens (Fig. 8b). Although the reinjected LLC cells were not completely eliminated, the proliferation of LLC cells was markedly reduced in the CAR-T+NVs@cGAMP-treated mice. A similar phenomenon was observed in the B16 tumor relapse model. This resistance to LLC or B16 cells in CAR-T+NVs@cGAMP-cured mice could be attributed to an enhanced epitope spreading phenomenon, whereby CAR-T cell-mediated lysis of tumor cells release a variety of neoantigens[61]. These cells are subsequently processed by antigen-presenting cells and presented to CAR-T cells, thereby enhancing CAR-T cell immune memory. Rechallenge with LLC or B16 cells promoted rapid proliferation of immune-memory CAR-T cells, thereby inhibiting the growth of B16 tumors in vivo. To further investigate whether CAR-T + NVs@cGAMP treatment induces epitope spreading, we established an LLC-MSLN-OVA tumor-bearing mouse model and implemented the same treatment regimen[12,47,54]. In this model, ovalbumin ($OVA_{257-264}$, SIINFEKL peptide) was introduced as a bystander antigen not targeted by MSLN-specific CAR-T cells. Fourteen days post-treatment, $CD8^+$ T cells were isolated from the spleens of mice for flow cytometric analysis. Mice treated with CAR-T + NVs@cGAMP exhibited a

significantly increased frequency of OVA-specific (SIINFEKL-directed) $CD8^+$ T cells compared to other treatment groups (Fig. 8c and Supplementary Fig. 27a). Additionally, upon in vitro stimulation of splenic $CD8^+$ T cells with the $OVA_{(257-264)}$ peptide, a higher proportion of IFN-γ^+ $CD8^+$ T cells was observed in the CAR-T + NVs@cGAMP-treated group (Fig. 8d and Supplementary Fig. 27b). These results suggest that CAR-T + NVs@cGAMP treatment promoted epitope spreading to non-MSLN antigens, thereby broadening the antitumor immune response. Survival curve analysis further supported these findings. In the LLC tumor relapse model, the survival rates of cured mice re-challenged with LLC-MSLN and LLC cells were 100% and 20%, respectively, within a period of 50 days. Similarly, in the B16 melanoma relapse model, survival rates were 100% for B16-MSLN and 60% for B16 cells (Fig. 8e).

Furthermore, we investigated whether combined treatment with CAR-T cells and aPD-L1 NVs@cGAMP inhibited ectopic tumor recurrence. After tumor eradication by CAR-T+NVs@cGAMP, ectopic tumor recurrence was mimicked by injecting LLC (or LLC-MSLN) cells and B16 (or B16-MSLN) cells into the inguinal region of cured mice from the LLC and B16 tumor models, respectively (Fig. 8f). Naive mice were used to control and received the same treatment. The IVIS results showed that the growth of LLC-MSLN cells in the groin was completely suppressed in the CAR-T+NVs@cGAMP-treated mice (Fig. 8g), indicating that CAR-T+NVs@cGAMP induced a systemic memory antitumor immune response. Similarly, the growth rate of LLC cells in the inguinal region was significantly lower in CAR-T +NVs@cGAMP-cured mice than in control mice, although the injected LLC cells were not completely eliminated. Consistent results were observed in the B16 tumor relapse model. Tumor volume measurements further confirmed that CAR-T + NVs@cGAMP treatment effectively inhibited the growth of both MSLN-positive and MSLN-negative tumor cells in the inguinal region across both models (Fig. 8h and Supplementary Fig. 28). Importantly, survival curve analysis revealed that compared with control mice, CAR-T +NVs@cGAMP-treated mice had a better survival rate in the ectopic recurrent tumor model (Fig. 8i). Furthermore, analysis of CAR-T cell proportions in peripheral blood at different time points revealed significant expansion of CAR-T cells in cured mice challenged with MSLN-overexpressing tumor cells in both models (Supplementary Figs. 29-30). This expansion contributed to the efficient clearance of the injected tumor cells. In contrast, cured mice challenged with parental tumor cells did not exhibit notable CAR-T cell expansion.

These results not only confirmed that CAR-T+NVs@cGAMP reversed the tumor microenvironment, but also highlighted its role in inducing epitope spreading in mouse tumor models. However, considering that the B16 and LLC models are quite different from human tumor patients in terms of tumor heterogeneity and tumor microenvironment, subsequent validation of these results in more complex models is needed, which is crucial for the future use of NVs@cGAMP to prevent tumor recurrence and improve the efficacy of CAR-T cell therapy[62–65].

Discussion

In this study, we aimed to address the dilemma of poor CAR-T cell efficacy against solid tumors by reversing the immunosuppressive tumor microenvironment into a tumor microenvironment favorable for CAR-T cell survival. To this end, we designed aPD-L1 NVs@cGAMP to deliver STING agonists to the lungs. Our results demonstrated that inhaled aPD-L1 NVs@cGAMP targeted STING agonist delivery to the lungs of tumor-bearing mice and induced the release of type I IFNs and chemokines, which in turn increased the infiltration of proinflammatory immune cells into tumor tissues. Importantly, the anti-PD-L1 scFv on the surface of aPD-L1 NVs@cGAMP effectively blocked the STING agonist-induced high expression of PD-L1 on the tumor surface, thereby preventing CAR-T cell exhaustion. In a mouse model of metastatic lung cancer, CAR-T+NVs@cGAMP not only eradicated established metastatic lung cancer in vivo, but also inhibited the growth of reinjected tumor cells. Thus, aPD-L1 NVs@cGAMP can effectively reverse the immunosuppressive tumor microenvironment and enhance the efficacy of CAR-T cells against solid tumors.

Compared to direct genetic modification of CAR-T cells, enhancing the efficacy of CAR-T cells by remodeling the tumor microenvironment with engineered nanovesicles has unique advantages. We and other teams have previously effectively enhanced the antitumor efficacy of CAR-T cells against solid tumors by engineering CAR-T cells with autocrine antibodies or cytokines[3,66,67]. However, we found that these additional modified genes not only reduce the expression efficiency of CAR proteins, but also may increase the burden of CAR-T cells, which is not conducive to maintaining the long-term activity of CAR-T cells. In addition, although enabling CAR-T cells to directly express pro-inflammatory cytokines can effectively enhance the activity of CAR-T cells, this sustained cytokine expression could lead to an uncontrollable cytokine storm and contribute to the rapid exhaustion of CAR-T cells[68–70]. In contrast, the present study utilized the strategy of engineered nanovesicles to modulate the tumor microenvironment and CAR-T cell activity, which was beneficial for maintaining a high CAR protein expression rate and T cell activity. Importantly, in future clinical applications, these engineered nanovesicles can be administered according to the activity of CAR-T cells in vivo, which in turn can precisely regulate CAR-T cell activity in real time and avoid uncontrollable cytokine storms. Thus, this strategy effectively balances CAR-T cell killing efficacy and safety.

When STING agonists are used to remodel the tumor microenvironment, a good delivery vehicle and route of administration will help them perform optimally. Although a number of STING agonists with potent immune-activating potency have been developed, there are still a number of challenges to their use in clinical trials[55,71–73]. First, because these free STING agonists still suffer from short half-lives, low cell permeability and poor tissue retention, high doses of STING agonists typically need to be administered intravenously to induce sufficiently potent antitumor immune responses. However, high concentrations of STING agonists tend to induce systemic inflammation. Although intratumoral injection can partially reduce the occurrence of excessive inflammation, rapid extravasation of STING agonists can still induce excessive activation of lymphocytes in organs such as the spleen[55]. In addition, intratumoral administration is not applicable to deep-seated tumors such as those of the lung. Second, due to the lack of targeting of STING agonists, high doses of STING may induce immune ablation characterized by progressive T-cell deficiency[73]. Finally, high levels of type I IFN induced by STING agonists tend to induce tumor cells to overexpress PD-L1, which in turn evades T cell killing[71]. To overcome these challenges, this study used nanovesicles expressing anti-PD-L1 scFvs to deliver STING agonists. Extracellular vesicles have been shown to be natural mediators that can deliver tumor cell-derived dsDNA to APCs to activate immune surveillance in tumor tissues[49,50]. Nanovesicles, as a kind of engineered cellular vesicles, not only inherit the advantages of natural extracellular vesicles with good biocompatibility, but also have the characteristics of high yield and easy modification[74,75]. Our results demonstrated that inhaled aPD-L1 NVs@cGAMP could rapidly accumulate in lung tissues and be taken up by tumor cells and DCs, and the presence of nanovesicles could still be detected in lung tissues 48 h after administration. These results suggest that nebulized delivery of aPD-L1 NVs@cGAMP effectively overcomes the problems of low cell permeability and poor tissue retention of STING agonists, and can activate the body's antitumor immune response at a low dose of STING agonists. Therefore, aPD-L1 NVs@cGAMP reduces the nonspecific uptake of STING agonists by T cells to a certain extent, and avoids T cell exhaustion caused by T cell uptake of high doses of STING agonists. However, it should be noted that nanovesicles as delivery vehicles also have their inherent

biophysical limitations[51,76,77]. For instance, the negative charge on the surface of nanovesicles may weaken their fusion with cell membranes. Additionally, challenges such as non-specific distribution during administration, inability to precisely release drugs, and clearance by the reticuloendothelial system (RES) need to be further addressed. In addition, aPD-L1 NVs@cGAMP required only 2% of the free STING agonist to induce a strong inflammatory immune response in tumor tissue and did not induce a systemic inflammatory response. However, it is important to acknowledge that the drug loading and encapsulation efficiencies of cGAMP in this study were relatively low. To improve the clinical translation and manufacturing feasibility of aPD-L1 NVs@cGAMP, further optimization of the drug loading conditions is necessary—such as increasing the concentration of cGAMP, altering the loading method, or adding fusion agents[78,79]. Importantly, the results demonstrated that aPD-L1 NVs@cGAMP effectively blocked the high expression of PD-L1 in tumor cells, thereby effectively preventing CAR-T cell exhaustion in tumor tissues. Thus, the strategy of delivering STING agonists using aPD-L1 NVs considerably improved the ability of STING agonists to remodel the tumor microenvironment.

However, many challenges remain to be overcome before aPD-L1 NVs@cGAMP can be used as an enhancer of CAR-T cells for clinical treatment. First, although this study has preliminarily investigated the biodistribution of aPD-L1 NVs@cGAMP after administration in a mouse model, comprehensive pharmacokinetic analyses in large mammals need to be further evaluated. Second, precise administration of aPD-L1 NVs@cGAMP based on the real-time activity of CAR-T cells was not performed in this study, and further optimization of the administration time and dose of aPD-L1 NVs@cGAMP is needed to achieve precise regulation of CAR-T cell activity. Finally, although the preliminary evaluation of CAR-T+NVs@cGAMP in this study revealed a favorable safety profile, the long-term effects of CAR-T+NVs@cGAMP on the immune system need to be further evaluated.

In conclusion, this study established a strategy to remodel the lung tumor microenvironment by inhalation of aPD-L1 NVs@cGAMP to enhance the efficacy of CAR-T cells against solid tumors. This strategy effectively balances the efficacy and safety of STING agonists in remodeling the tumor microenvironment, which in turn achieves long-term, mild enhancement of CAR-T cell activity. Therefore, aPD-L1 NVs@cGAMP is expected to serve as a potent CAR-T cell enhancer to help CAR-T cells break through the inhibition of the tumor microenvironment and dramatically increase the killing efficacy of CAR-T cells against lung tumors.

Methods

Ethical statement

Our study was conducted in strict accordance with all relevant ethical standards and institutional guidelines. All animal experimental protocols were carried out in compliance with the Guide for the Care and Use of Laboratory Animals and received approval from the Animal Care and Use Committee of the Fifth Affiliated Hospital of Sun Yat-sen University. Female C57BL/6 mice (4–6 weeks old) were obtained from the Guangdong Medical Laboratory Animal Center. The mice were housed in an environment maintained at approximately 25 °C with 50% relative humidity and subjected to a 12-hour light-dark cycle. They had free access to standard laboratory chow and water. For the in situ and metastatic lung cancer models, no specific maximum tumor size was imposed, provided that animals were euthanized as soon as they reached a predetermined humane endpoint, thus prioritizing their welfare. In contrast, for the subcutaneous tumor model, a strict upper limit of 2000 mm^3 was set on tumor volume. No animal in this study exceeded that limit. Euthanasia was performed via cervical dislocation under deep anesthesia. Sex was not explicitly considered in our study design for animal experiments due to lung cancer affecting people of the male and female sex.

Cells and plasmids

293 T (human embryonic kidney cell line), LLC (Lewis lung carcinoma) and B16-F10 (mouse melanoma) cells were purchased from ATCC, PC-9 (lung adenocarcinoma) were supplied by the Chinese Academy of Sciences. and all three cell lines were cultured in Dulbecco's modified Eagle's medium (DMEM, Thermo Fisher Scientific) supplemented with 10% fetal bovine serum (FBS, Invitrogen). Nucleotide sequences encoding anti-PD-L1 scFv and MSLN were synthesized by BGI (Beijing, China) and cloned and inserted into the pCDH-CMV-P2A-EGFP-EF1a-Puro and pCDH-CMV-P2A-fLuc-EF1a-Puro vectors, respectively. The resulting target plasmids were mixed with the helper plasmids pMD2. G (12259; Addgene) and psPAX2 (12260; Addgene) at a 4:1:3 ratio and co-transfected into 293 T cells with polyethyleneimine (PEI) to obtain lentiviruses encoding anti-PD-L1 scFv and MSLN. After infecting 293 T cells with the lentivirus encoding anti-PD-L1 scFv and selecting with puromycin, we obtained 293 T cells stably expressing anti-PD-L1 scFv (designated as aPD-L1 293 T). Similarly, LLC and B16 cells were infected with the lentivirus encoding MSLN and selected with puromycin to generate LLC-MSLN and B16-MSLN cells, respectively, which stably express MSLN. LLC cells stably expressing both MSLN and ovalbumin (OVA) were obtained using a similar method and designated LLC-MSLN-OVA cells.

Preparation and characteristics of MSLN CAR-T cells

MSLN CAR-T cells were prepared following previous reports[40]. Briefly, the nucleotide sequence encoding anti-human MSLN-scFv was synthesized by BGI and cloned and inserted into the pLV-EF1a-MYC-EGFP vector to obtain the pLV-MSLN CAR plasmid. The pLV-MSLN CAR was mixed with the helper plasmids pMD2. G and psPAX2 at a 4:1:3 ratio and co-transfected with PEI into 293 T cells to obtain the CAR lentivirus.

T cells isolated from mouse spleens were cultured in serum-free cell culture medium (Basso Cell Technology Co., Ltd., Zhuhai, China) supplemented with 5% FBS and 150 U/mL recombinant IL-2 (PeproTech) and activated using anti-CD28 and anti-CD3 monoclonal antibodies (PeproTech, USA). The next day, the prepared CAR lentivirus was transfected into T cells to obtain MSLN CAR-T cells. MOCK-T cells were obtained using the same preparation method. The expression efficiency of the CAR protein on T cells was analyzed by flow cytometry[80]. Specifically, T cells transduced for 7 days were washed with PBS and resuspended. We then incubated 1×10^6 cells with 1 µL of Protein L (1 mg/mL) at 4°C for 30 minutes. Protein L binds specifically to the kappa light chain of the scFv region in the CAR construct, enabling the detection of CAR expression. After incubation, the cells were washed three times with PBS containing 1% bovine serum albumin (BSA). The samples were then stained with PE-conjugated streptavidin (BioLegend, San Diego, CA, USA) and washed three more times. Finally, the cells were analyzed using a CytoFLEX LX flow cytometer (Beckman Coulter, Atlanta, GA, USA). To determine the ability of MSLN CAR-T cells to target B16-MSLN cells, MSLN CAR-T cells or MOCK-T cells were co-incubated with B16-MSLN cells at different potency-to-target ratios (0.5, 1, 2 and 5), and then, confocal microscopy was used to visualize the lysis of B16-MSLN cells. In addition, the killing efficiency of CAR-T cells against B16-MSLN and PC-9 cells was assessed using an LDH kit (Promega, UK) according to the manufacturer's instructions.

Preparation of aPD-L1 NVs@cGAMP

aPD-L1 NVs were prepared from aPD-L1 293 T cells[37]. Briefly, after PBS-washed aPD-L1 293 T cells were resuspended in hypotonic lysis buffer (1 mM NaHCO3, 0.2 mM EDTA and 1 mM PMSF) and lysed for 12 h at 4°C, the lysed cells were ground at least 20 times using a Dounce homogenizer. The ground mixture was centrifuged at 2,000×g for 5 min to remove large amounts of cellular debris, the collected supernatant was centrifuged at 10,000 × g for 30 min to remove the precipitate, and finally, the collected supernatant was centrifuged at

100,000 × *g* for 90 min to obtain a gray–white cell membrane precipitate. The aPD-L1 NVs were obtained by sequentially passing the obtained cell membranes through 800 nm and 200 nm polycarbonate membranes using an extruder (Avanti Polar Lipids). The protein concentration of the PD-L1 NVs was quantified using a BCA protein kit.

The morphology and size of the aPD-L1 NVs were visualized by transmission electron microscopy. Briefly, 15 μL of nanovesicles resuspended in PBS were dropped onto a copper grid and negatively stained with 2% dicumyl acetate. After air drying, the samples were scanned with a transmission electron microscope (JM-1400; JEOL, Japan) at 120 kV. The particle concentration and size distribution of the aPD-L1 NVs were measured using a NanoSight NS300 system (Malvern Instruments Company, UK), and the data were analyzed using NTA 3.1 software. The zeta potential of the aPD-L1 NVs was detected using DLS (ZEN 3600 Zetasizer, Malvern).

The loading of aPD-L1 NVs on STING agonists and the quantification of STING agonists were performed according to previously published literature. Briefly, after mixing 1, 2, 4, 8, and 16 mM cGAMP (InvivoGen) with aPD-L1 NVs and co-incubating at 37°C for 24 h, the nanovesicles were centrifuged at 100,000 × *g* for 60 min using an Optima XE-100 (Beckman) to obtain concentrated nanovesicles. The obtained nanovesicle precipitates were washed once with PBS, resuspended in PBS, and stored at −80 °C.

Characterization of anti-PD-L1 scFv expression in aPD-L1 293 T cells and nanovesicles

In this study, we employed Protein L to detect the presence of anti-PD-L1 scFv on the surfaces of aPD-L1 293 T cells and aPD-L1 NVs. Protein L specifically binds to the κ light chain of the scFv region, making it an effective tool for detecting scFv fragments and chimeric antigen receptors (CARs) expressed on cell membranes. To detect anti-PD-L scFv on the surface of aPD-L1 293 T cells, we incubated 1×10^6 cells with 1 μL Protein L (1 mg/mL, GenScript) at 4 °C for 30 minutes, followed by washing with PBS. The cells were then stained with PE-conjugated streptavidin (BioLegend, San Diego, CA, USA) and analyzed using a CytoFLEX LX flow cytometer (Beckman Coulter, Atlanta, GA, USA).

To facilitate the detection of anti-PD-L1 scFv on NVs, we incubated 20 μL of nanovesicles with 10 μL of 4 μm aldehyde/sulfate latex beads (Invitrogen) at room temperature for 15 minutes. We then added 1 mL PBS and rotated the mixture for 2 hours to allow efficient coupling of the nanovesicles to the beads. After adding 110 μL glycine (100 mM) and incubating for 30 minutes, the bead-bound nanovesicles were collected by centrifugation. The samples were then stained with Protein L and PE-conjugated streptavidin as described above and analyzed by flow cytometry.

To confirm the functional expression of anti-PD-L1 scFv on aPD-L1 293 T cells, an in vitro binding assay was performed. This assay evaluated the ability of aPD-L1 293 T cells to bind recombinant PD-L1 protein, thereby verifying the antigen-binding functionality of the expressed scFv. 293 T cells stably expressing only GFP (293T-GFP) were used as a control. Both 293T-GFP and aPD-L1 293 T cells were incubated with 10 μg/mL recombinant PD-L1 protein for 4 hours. After washing away unbound PD-L1 protein, the cells were stained with Alexa Fluor® 647-conjugated anti-PD-L1 antibody and examined using confocal microscopy.

In vivo biodistribution of aPD-L1 NVs@cGAMP

To assess aPD-L1 NVs@cGAMP in vivo biodistribution, aPD-L1 NVs@cGAMP were labeled with DiR dye (Abmole, USA) according to the manufacturer's instructions. Briefly, DiR-labeled aPD-L1 NVs@cGAMP were obtained after co-incubating aPD-L1 NVs@cGAMP with DIR dye for 30 min and centrifuging at 150,000 × g for 80 min using an ultrahigh-speed centrifuge to remove free dye. Twelve hours after the administration of 200 μg of DiR-labeled aPD-L1 NVs@cGAMP via nebulization or tail vein injection, fluorescence quantification of the major organs of the collected mice was performed using an IVIS imaging system. Twelve hours after the administration of 200 μg of DiI-labeled aPD-L1 NVs@cGAMP via nebulization or tail vein injection, mouse lung tissues were collected and stained for tissue immunofluorescence to visually assess the distribution of aPD-L1 NVs@cGAMP in the lungs. Confocal microscopy was used to examine the distribution of aPD-L1 NVs@cGAMP in lung tissue sections. The pulmonary vasculature was labeled with an anti-CD31 antibody. In addition, the uptake of DiI-labeled aPD-L1 NVs@cGAMP by different cells in the tumor microenvironment was analyzed by flow cytometry. To investigate the dose dependence of aPD-L1 NVs@cGAMP biodistribution in vivo, mice were nebulized with 25 μg, 50 μg, 100 μg or 200 μg of DiR-labeled aPD-L1 NVs@cGAMP, and fluorescence quantification of major organs was performed using the IVIS imaging system after 12 hours. To investigate the time dependence of aPD-L1 NVs@cGAMP biodistribution in vivo, mice were nebulized with 200 μg of DiR-labeled aPD-L1 NVs@cGAMP. Fluorescence quantification of the major organs of the mice was performed using an IVIS imaging system at 6, 12, 24 and 48 hours.

Western blot analysis

Western blot analysis was performed to detect the expression of the anti-PD-L1 scFv protein in engineered 293 T cells and nanovesicles. In this study, the anti-PD-L1 scFv protein was tagged with a Myc epitope tag, enabling detection using an anti-Myc monoclonal antibody. Briefly, cells and nanovesicles were lysed using RIPA buffer before the total protein concentration was determined using a BCA protein assay kit (Pierce, USA). After equal amounts of proteins were separated and transferred to polyvinylidene difluoride (PVDF) membranes via 10% SDS–PAGE, the PVDF membranes were blocked with 5% skim milk powder and washed with PBST (PBS containing 0.1% Tween-20). After blocking, the membranes were washed with PBST and incubated overnight at 4°C with primary antibodies: mouse anti-Myc-Tag monoclonal antibody (9B11, Cell Signaling Technology) to detect the anti-PD-L1 scFv protein, and rabbit anti-β-actin monoclonal antibody (13E5, Cell Signaling Technology) as a loading control. Following three washes with TBST (Tris-buffered saline with 0.1% Tween-20), the membranes were incubated with HRP-conjugated secondary antibodies for 1 hour at room temperature. After additional washes with TBST, the protein bands were visualized using the ECL Prime chemiluminescent reagent (GE Healthcare) and ImageQuant LAS 500 (Cytiva).

Assessment of NVs@cGAMP on MSLN CAR-T cell cytotoxicity and proliferation

The effect of NVs@cGAMP on the cytotoxicity of MSLN CAR-T cells was evaluated as previously described[81–83]. Briefly, 2×10^4 luciferase-expressing LLC-MSLN cells, 1×10^4 CAR-T cells, and 2×10^3 dendritic cells were seeded into white opaque 96-well plates. Different treatments were added as required, and the cells were incubated at 37 °C with 5% CO_2 for 12 hours. Wells containing LLC-MSLN cells alone (without effector cells) served as positive controls to determine maximum luciferase activity. After co-incubation, the supernatant was gently removed, and cell lysis buffer (Promega) was added according to the manufacturer's instructions, followed by the addition of 10 μL Steady-Glo luciferase substrate (Promega). After a 5-minute incubation, luminescence was measured using an EnVision multimode plate reader (PerkinElmer). The cytotoxicity of CAR-T cells was calculated based on the luminescence readings using the following formula: % Killing = 100− [(RLU from co-culture wells/RLU from control wells) × 100].

For proliferation assessment, LLC-MSLN cells, GFP-expressing CAR-T cells, and dendritic cells were seeded into 12-well plates at a ratio of 10:5:1. Different treatments were added as required, and the cells were incubated at 37 °C with 5% CO_2 for 5 days. During this period,

the culture medium was refreshed as necessary based on the proliferation rate of CAR-T cells to ensure adequate nutrient supply. After 5 days, cells were harvested and counted using flow cytometry.

Evaluation of cytokine expression levels

The effects of aPD-L1 NVs@cGAMP on cytokine levels in the tumor microenvironment were evaluated by qPCR and ELISA. Briefly, mice were randomly divided into four groups and given inhaled PBS, aPD-L1 NVs, cGAMP or aPD-L1 NVs@cGAMP, and six hours later, mouse lungs were harvested for gene expression analysis. Total RNA was extracted from the lysed lung tissue using TRIzol reagent according to the manufacturer's protocol, and the RNA concentration was quantified using a NanoDrop spectrophotometer. Then, the RNA was reverse transcribed to cDNA using a RevertAid First Strand cDNA Synthesis Kit. The primers, cDNA, and SYBR Green Master Mix (Applied Biosystems) were mixed, and RT–qPCR was performed using a CFX96 Real-Time PCR System (Bio-Rad). The DNA sequences of the primers used in this study were synthesized by BGI Tech (Shenzhen, China) and are listed in Supplementary Table 1.

Additionally, we evaluated whether aPD-L1 NVs@cGAMP could retain its STING agonist activity after different storage durations at −80 °C using qPCR. Specifically, DCs were co-incubated with aPD-L1 NVs@cGAMP stored for varying periods, and after 12 hours, DCs were collected. The mRNA expression levels of *IFNB1, IFIT1, IFIT2, and ISG15* were measured as described above. DCs treated with PBS and aPD-L1 NVs (nanovesicles without cGAMP) served as negative control groups.

Furthermore, lung and serum samples from different groups of mice were collected and tested for the expression of IL-1β, IL-6, IL-7, IL-10, IL-12, IL-15, TGF-β, TNF-α, IFN-γ and IFN-β according to the instructions of the ELISA kit manufacturer.

Tissue Immunostaining

The expression of inducible nitric oxide synthase (iNOS) and cyclooxygenase-2 (COX-2) in tumor tissues from tumor-bearing mice was detected through immunohistochemistry (IHC). Briefly, after 14 days of treatment in LLC-MSLN tumor-bearing mice, the mice were euthanized, and lung tissues were collected. The tissues were processed into paraffin-embedded sections and underwent antigen retrieval following standard protocols[81]. The prepared lung tissue sections were incubated overnight at 4 °C with primary antibodies: anti-iNOS (Proteintech, clone: 6O22, dilution 1:1000) and anti-COX-2 (Proteintech, clone: 3G2B9, dilution 1:1000). Following primary antibody incubation, sections were stained with appropriate secondary antibodies to visualize the proteins of interest.

Detection of co-expression of CD31 and PD-L1 in tumor tissues was performed similarly, using primary antibodies anti-PD-L1 (Proteintech, clone: 2B11D11) and anti-CD31 (Abcam, clone: EPR17259). The stained sections were analyzed using a digital slide scanner (P250 FLASH).

Flow cytometry analysis of immune cells

To evaluate the effects of various agents on immune cells in the tumor microenvironment, isolated tumor tissues were mechanically separated into small pieces and digested in DMEM containing type IV collagenase (1 mg/mL, Sigma–Aldrich) for 30 min. Then, the digested tumor tissues were filtered through a 70-μm cell filter (Beyotime), and erythrocytes were lysed with erythrocyte lysis solution to obtain a single-cell suspension. To block the nonspecific binding sites of the cells, all cell samples were pretreated with anti-mouse CD16/32. For further analysis by flow cytometry, the prepared tumor cell suspensions were stained with the following antibodies: anti-CD3-APC (clone: 17A2), anti-CD8-Pacific Blue (clone: 53-6.7), anti-CD8-PE (clone: 53-6.7), CD4-FITC (clone: GK1.5), anti-CD45-PE/Cyanine7 (clone: 30-F11), anti-PD-1-FITC (clone: 29F.1A12), anti-LAG-3-Brilliant Violet (clone: C9B7W), anti-TIGIT-PE (clone: 1G9), anti-TIM-3-APC (clone: B8.2C12) and anti-Granzyme B-PE (clone: QA16A02) for T cell analysis; anti-CD44-FITC (BioLegend, Clone: IM7) and anti-CD62L-APC (BioLegend, Clone: MEL-14) for memory T cells; anti-CD80-APC (clone: 16-10A1) and anti-CD86-PE (clone: GL-1) for mature DC analysis; anti-Foxp3-PE (clone: MF14) and anti-CD25-PerCP/Cyanine5.5 (clone: PC61); and anti-CD11b-Pacific Blue (clone: M1/70) and anti-Gr1-APC/Cyanine 7 (clone: RB6-8C5) for MDSC analysis; anti-IFN-γ-FITC (clone: XMG1.2), anti-IL-4-PE/Cyanine7 (clone: 11B11) and anti-IL-17A-Brilliant Violet 421 (clone: TC11-18H10.1) for Th cells analysis; and anti-F4/80-PerCP/Cyanine5.5 (clone: BM8) for macrophage analysis. The above antibodies were purchased from BioLegend. To evaluate NVs@cGAMP-induced epitope spreading, T cells isolated from the spleen were stained with PE-conjugated H-2Kb/OVA (SIINFEKL) tetramer (MBL, TB-5001-1) to detect SIINFEKL-specific CD8 + T cells[12]. Additionally, 1×10^6 $CD8^+$ T cells were incubated with SIINFEKL peptide to stimulate antigen-specific T cells, and flow cytometry was used to detect IFN-γ-expressing $CD8^+$ T cells. The stained samples were analyzed using an Attune NxT flow cytometer, and the obtained data were analyzed using FlowJo software (Tree Star, Ashland, OR). The gating strategy for flow cytometry is shown in Supplementary Fig. 31 and Supplementary Fig. 32.

Evaluation of the ability of aPD-L1 NVs@cGAMP to enhance the antitumor potency of CAR-T cells in vivo

To evaluate the antitumor potency of aPD-L1 NVs@cGAMP in enhancing CAR-T cells in vivo, we established LLC-MSLN orthotopic lung cancer mouse models and B16-MSLN metastatic lung cancer mouse models. Briefly, 5-week-old female C57BL/6 mice were obtained from the Guangdong Medical Laboratory Animal Center. To construct the orthotopic tumor model, mice were anesthetized with 2% isoflurane, and a 5 mm skin incision was made on the left chest, approximately 1 cm anterior to the left axilla. Muscles and fat were separated to expose lung movement. Subsequently, 0.5×10^6 luciferase-expressing LLC-MSLN cells suspended in 50 μL of DMEM/matrigel were rapidly injected into the left lung tissue at a depth of 3 mm. The incision was sutured, and topical antibiotics (gentamicin and erythromycin) were applied to prevent postoperative infection. Animals were observed for 45 to 60 minutes until full recovery[37]. A total of 0.5×10^6 luciferase-expressing B16-MSLN cells were injected into C57BL/6 mice via the tail vein, and the in vivo bioluminescence of the mice was measured using the IVIS system to evaluate whether metastatic lung cancer was successfully established.

Seven days post-tumor cell inoculation, mice with established LLC-MSLN orthotopic tumors and B16-MSLN metastatic tumors were randomized into different treatment groups to receive the respective drug regimens, including aPD-L1 NVs@cGAMP, CAR-T cells, or combination therapy. To evaluate the growth of tumor cells in vivo, D-luciferin (150 mg/kg, Abmole, USA) was injected into mice transperitoneally on days 0, 7, and 14 after drug administration, and the bioluminescence of tumors was detected by an IVIS imaging system. Mice were sacrificed for observation of tumor cell metastasis in the lungs on day 14 post-treatment. Throughout the experimental period, the weight changes and survival rates of the mice were recorded in detail. In this study, each mouse within the same group was independently subjected to the same treatment, making each mouse a biological replicate. Thus, the IVIS imaging experiments and survival rate analyses included 4 and 10 biological replicates, respectively.

To evaluate the inhibitory effects of the combined therapy on tumor recurrence, mice that achieved complete tumor remission were rechallenged on day 28 post-treatment initiation. In the LLC-MSLN model, cured mice were inoculated either orthotopically or subcutaneously in the inguinal region with 0.5×10^6 LLC-MSLN or parental LLC cells to simulate local and distant tumor recurrence. In the B16-MSLN model, cured mice were injected via the tail vein or subcutaneously in the inguinal region with 0.5×10^6 B16-MSLN or parental

B16 cells. Untreated mice receiving the same tumor cell inoculations served as controls. Untreated mice were challenged with the same tumor cells to serve as controls. Similarly, tumor growth and survival were monitored in vivo in tumor-bearing mice as described above. All of the above animal experiments were conducted in accordance with the animal care and use regulations of the Fifth Hospital of Sun Yat-sen University.

Safety evaluation

Serum biochemical parameters and histomorphology of major organs were evaluated in mice to assess the biocompatibility of CAR-T+NVs@cGAMP. Briefly, C57BL/6 mice were randomized into 2 groups and treated with 200 μL PBS or CAR-T+NVs@cGAMP on days 0 and 3. Mice were euthanized on day 14, and serum was collected to assess changes in liver and kidney function. Serum biochemical parameters, including alanine aminotransferase (ALT), aspartate aminotransferase (AST), alkaline phosphatase (ALP), blood urea nitrogen (BUN), creatinine (CR), globulin (GLB), albumin (ALB), cholesterol (Chol), triglyceride (TG), and total bilirubin (TBIL), were measured using commercially available test kits. In addition, the collected mouse organs were fixed with 4% paraformaldehyde and then stained with hematoxylin and eosin (H&E) to observe the effect of CAR-T+NVs@cGAMP on the histomorphology of major organs in mice.

Statistical analysis

All the data in this study were analyzed using GraphPad Prism 8.0. Differences between two groups were analyzed using Student's t-test, and differences among multiple groups were analyzed using one-way ANOVA and Tukey's test. All results are expressed as the mean ± standard deviation (SD). Survival curves were analyzed by Kaplan–Meier analysis. $p < 0.05$ was considered to indicate statistical significance.

Reporting summary

Further information on research design is available in the Nature Portfolio Reporting Summary linked to this article.

Data availability

All relevant data are available within the Article, Supplementary Information or Source Data file. Source data are provided with this paper and are also available in Figshare: https://doi.org/10.6084/m9.figshare.27901938.

References

1. Young, R. M., Engel, N. W., Uslu, U., Wellhausen, N. & June, C. H. Next-Generation CAR T-cell Therapies. *Cancer Discov.* **12**, 1625–1633 (2022).
2. Flugel, C. L. et al. Overcoming on-target, off-tumour toxicity of CAR T cell therapy for solid tumours. *Nat. Rev. Clin. Oncol.* **20**, 49–62 (2023).
3. Labanieh, L. & Mackall, C. L. CAR immune cells: design principles, resistance and the next generation. *Nature* **614**, 635–648 (2023).
4. Albelda, S. M. CAR T cell therapy for patients with solid tumours: key lessons to learn and unlearn. *Nat. Rev. Clin. Oncol.* **21**, 47–66 (2024).
5. Hou, A. J., Chen, L. C. & Chen, Y. Y. Navigating CAR-T cells through the solid-tumour microenvironment. *Nat. Rev. Drug. Discov.* **20**, 531–550 (2021).
6. Landoni, E. et al. IL-12 reprograms CAR-expressing natural killer T cells to long-lived Th1-polarized cells with potent antitumor activity. *Nat. Commun.* **15**, 89 (2024).
7. Lee, D. et al. Unlocking the potential of allogeneic Vdelta2 T cells for ovarian cancer therapy through CD16 biomarker selection and CAR/IL-15 engineering. *Nat. Commun.* **14**, 6942 (2023).
8. Ma, L. et al. Enhanced CAR-T cell activity against solid tumors by vaccine boosting through the chimeric receptor. *Science* **365**, 162–168 (2019).
9. Mackensen, A. et al. CLDN6-specific CAR-T cells plus amplifying RNA vaccine in relapsed or refractory solid tumors: the phase 1 BNT211-01 trial. *Nat. Med.* **29**, 2844–2853 (2023).
10. Ogunnaike, E. A. et al. Fibrin gel enhances the antitumor effects of chimeric antigen receptor T cells in glioblastoma. *Sci. Adv.* **7**, eabg5841 (2021).
11. Agliardi, G. et al. Intratumoral IL-12 delivery empowers CAR-T cell immunotherapy in a pre-clinical model of glioblastoma. *Nat. Commun.* **12**, 444 (2021).
12. Jin, C., Ma, J., Ramachandran, M., Yu, D. & Essand, M. CAR T cells expressing a bacterial virulence factor trigger potent bystander antitumour responses in solid cancers. *Nat. Biomed. Eng.* **6**, 830–841 (2022).
13. Li, H. et al. Targeting brain lesions of non-small cell lung cancer by enhancing CCL2-mediated CAR-T cell migration. *Nat. Commun.* **13**, 2154 (2022).
14. Luke, J. J. et al. The PD-1- and LAG-3-targeting bispecific molecule tebotelimab in solid tumors and hematologic cancers: a phase 1 trial. *Nat. Med.* **29**, 2814–2824 (2023).
15. Miller, I. C. et al. Enhanced intratumoural activity of CAR T cells engineered to produce immunomodulators under photothermal control. *Nat. Biomed. Eng.* **5**, 1348–1359 (2021).
16. Rafiq, S. et al. Targeted delivery of a PD-1-blocking scFv by CAR-T cells enhances anti-tumor efficacy in vivo. *Nat. Biotechnol.* **36**, 847–856 (2018).
17. Eckman, N., Nejatfard, A., Cavet, R., Grosskopf, A. K. & Appel, E. A. Biomaterials to enhance adoptive cell therapy. *Nat. Rev. Bioeng.* **2**, 408–424 (2024).
18. Liao, Z. et al. Lymph node-biomimetic scaffold boosts CAR-T therapy against solid tumor. *Natl. Sci. Rev.* **11**, nwae018 (2024).
19. Shi, J. et al. Lyophilized lymph nodes for improved delivery of chimeric antigen receptor T cells. *Nat. Mater.* **23**, 844–853 (2024).
20. An, J. et al. Enhancement of the viability of T cells electroporated with DNA via osmotic dampening of the DNA-sensing cGAS-STING pathway. *Nat. Biomed. Eng.* **8**, 149–164 (2024).
21. Dosta, P. et al. Investigation of the enhanced antitumour potency of STING agonist after conjugation to polymer nanoparticles. *Nat. Nanotechnol.* **18**, 1351–1363 (2023).
22. Falahat, R. et al. Epigenetic reprogramming of tumor cell-intrinsic STING function sculpts antigenicity and T cell recognition of melanoma. *Proc. Natl. Acad. Sci. USA* **118**, e2013598118 (2021).
23. Xu, N. et al. STING agonist promotes CAR T cell trafficking and persistence in breast cancer. *J. Exp. Med.* **218**, e20200844 (2021).
24. Jneid, B. et al. Selective STING stimulation in dendritic cells primes antitumor T cell responses. *Sci. Immunol.* **8**, eabn6612 (2023).
25. Wu, Y. T. et al. Tumor-targeted delivery of a STING agonist improvescancer immunotherapy. *Proc. Natl. Acad. Sci. USA* **119**, e2214278119 (2022).
26. Zhang, P. et al. STING agonist-loaded, CD47/PD-L1-targeting nanoparticles potentiate antitumor immunity and radiotherapy for glioblastoma. *Nat. Commun.* **14**, 1610 (2023).
27. Samson, N. & Ablasser, A. The cGAS-STING pathway and cancer. *Nat. Cancer* **3**, 1452–1463 (2022).
28. Vornholz, L. et al. Synthetic enforcement of STING signaling in cancer cells appropriates the immune microenvironment for checkpoint inhibitor therapy. *Sci. Adv.* **9**, eadd8564 (2023).
29. Wang, K. et al. Gas therapy potentiates aggregation-induced emission luminogen-based photoimmunotherapy of poorly immunogenic tumors through cGAS-STING pathway activation. *Nat. Commun.* **14**, 2950 (2023).

30. Wang Y., et al. Universal STING mimic boosts antitumour immunity via preferential activation of tumour control signalling pathways. *Nat. Nanotechnol.* (2024).
31. Koo, S. et al. Ceria-vesicle nanohybrid therapeutic for modulation of innate and adaptive immunity in a collagen-induced arthritis model. *Nat. Nanotechnol.* **18**, 1502–1514 (2023).
32. Liu, C. et al. A nanovaccine for antigen self-presentation and immunosuppression reversal as a personalized cancer immunotherapy strategy. *Nat. Nanotechnol.* **17**, 531–540 (2022).
33. Wang, L. et al. Bioinspired engineering of fusogen and targeting moiety equipped nanovesicles. *Nat. Commun.* **14**, 3366 (2023).
34. Wang, Z. et al. Sphingomyelin-derived nanovesicles for the delivery of the IDO1 inhibitor epacadostat enhance metastatic and post-surgical melanoma immunotherapy. *Nat. Commun.* **14**, 7235 (2023).
35. Zhou, M. et al. Nanovesicles loaded with a TGF-beta receptor 1 inhibitor overcome immune resistance to potentiate cancer immunotherapy. *Nat. Commun.* **14**, 3593 (2023).
36. Chen Y. et al. An oncolytic virus-T cell chimera for cancer immunotherapy. *Nat. Biotechnol.* (2024).
37. Li, X. et al. Genetically Programmable Vesicles for Enhancing CAR-T Therapy against Solid Tumors. *Adv. Mater.* **35**, e2211138 (2023).
38. Xiao, Y. et al. Functionalized biomimetic nanoparticles combining programmed death-1/programmed death-ligand 1 blockade with photothermal ablation for enhanced colorectal cancer immunotherapy. *Acta. Biomater.* **157**, 451–466 (2023).
39. Zheng, W. et al. Inhalable CAR-T cell-derived exosomes as paclitaxel carriers for treating lung cancer. *J. Transl. Med.* **21**, 383 (2023).
40. Zhu, T., Chen, Z., Jiang, G. & Huang, X. Sequential Targeting Hybrid Nanovesicles Composed of Chimeric Antigen Receptor T-Cell-Derived Exosomes and Liposomes for Enhanced Cancer Immunochemotherapy. *ACS Nano* **17**, 16770–16786 (2023).
41. Kang, M., Jordan, V., Blenkiron, C. & Chamley, L. W. Biodistribution of extracellular vesicles following administration into animals: A systematic review. *J. Extracell. Vesicles* **10**, e12085 (2021).
42. Liu M., Hu S., Yan N., Popowski K. D., Cheng K. Inhalable extracellular vesicle delivery of IL-12 mRNA to treat lung cancer and promote systemic immunity. *Nat. Nanotechnol.* (2024).
43. Boswell, C. A. et al. Effects of charge on antibody tissue distribution and pharmacokinetics. *Bioconjug. Chem.* **21**, 2153–2163 (2010).
44. Gupta, P. et al. Antibodies with weakly basic isoelectric points minimize trade-offs between formulation and physiological colloidal properties. *Mol. Pharm.* **19**, 775–787 (2022).
45. Liu, S., Verma, A., Kettenberger, H., Richter, W. F. & Shah, D. K. Effect of variable domain charge on in vitro and in vivo disposition of monoclonal antibodies. *MAbs* **13**, 1993769 (2021).
46. Miller, T. J. et al. PD-L1+ dendritic cells in the tumor microenvironment correlate with good prognosis and CD8+ T cell infiltration in colon cancer. *Cancer Sci.* **112**, 1173–1183 (2021).
47. Lai, J. et al. Adoptive cellular therapy with T cells expressing the dendritic cell growth factor Flt3L drives epitope spreading and antitumor immunity. *Nat. Immunol.* **21**, 914–926 (2020).
48. Li, G. et al. cGAS-STING pathway mediates activation of dendritic cell sensing of immunogenic tumors. *Cell Mol. Life Sci.* **81**, 149 (2024).
49. McAndrews, K. M., Che, S. P. Y., LeBleu, V. S. & Kalluri, R. Effective delivery of STING agonist using exosomes suppresses tumor growth and enhances antitumor immunity. *J. Biol. Chem.* **296**, 100523 (2021).
50. Jang, S. C. et al. ExoSTING, an extracellular vesicle loaded with STING agonists, promotes tumor immune surveillance. *Commun. Biol.* **4**, 497 (2021).
51. Zhang, E., Phan, P. & Zhao, Z. Cellular nanovesicles for therapeutic immunomodulation: A perspective on engineering strategies and new advances. *Acta Pharm. Sin. B.* **13**, 1789–1827 (2023).
52. Shi, M. M. et al. Preclinical efficacy and clinical safety of clinical-grade nebulized allogenic adipose mesenchymal stromal cells-derived extracellular vesicles. *J. Extracell Vesicles* **10**, e12134 (2021).
53. Uslu, U. et al. The STING agonist IMSA101 enhances chimeric antigen receptor T cell function by inducing IL-18 secretion. *Nat. Commun.* **15**, 3933 (2024).
54. Conde, E. et al. Epitope spreading driven by the joint action of CART cells and pharmacological STING stimulation counteracts tumor escape via antigen-loss variants. *J. Immunother. Cancer* **9**, e003351 (2021).
55. Chin, E. N., Sulpizio, A. & Lairson, L. L. Targeting STING to promote antitumor immunity. *Trends Cell Biol.* **33**, 189–203 (2023).
56. Golubovskaya, V. & Wu, L. Different subsets of T cells, memory, effector functions, and CAR-T immunotherapy. *Cancers (Basel)* **8**, 36 (2016).
57. Basu, A. et al. Differentiation and regulation of T(H) cells: a balancing act for cancer immunotherapy. *Front Immunol.* **12**, 669474 (2021).
58. Li, C., Jiang, P., Wei, S., Xu, X. & Wang, J. Regulatory T cells in tumor microenvironment: new mechanisms, potential therapeutic strategies and future prospects. *Mol. Cancer* **19**, 116 (2020).
59. Guery, L. & Hugues, S. Th17 Cell Plasticity and Functions in Cancer Immunity. *Biomed. Res. Int.* **2015**, 314620 (2015).
60. Farber, D. L. Form and function for T cells in health and disease. *Nat. Rev. Immunol.* **20**, 83–84 (2020).
61. Ma, L. et al. Vaccine-boosted CAR T crosstalk with host immunity to reject tumors with antigen heterogeneity. *Cell* **186**, 3148–3165 e3120 (2023).
62. Barutello, G. et al. Strengths and weaknesses of pre-clinical models for human melanoma treatment: dawn of dogs' revolution for immunotherapy. *Int. J. Mol. Sci.* **19**, 799 (2018).
63. Guerin, M. V., Finisguerra, V., Van den Eynde, B. J., Bercovici, N. & Trautmann, A. Preclinical murine tumor models: a structural and functional perspective. *Elife* **9**, e50740 (2020).
64. Overwijk W. W., Restifo N. P. B16 as a mouse model for human melanoma. *Curr. Protoc. Immunol.* **Chapter 20**, Unit 20 21 (2001).
65. Patton, E. E. et al. Melanoma models for the next generation of therapies. *Cancer Cell* **39**, 610–631 (2021).
66. Chen, J. et al. Target delivery of a PD-1-TREM2 scFv by CAR-T cells enhances anti-tumor efficacy in colorectal cancer. *Mol. Cancer* **22**, 131 (2023).
67. Gumber, D. & Wang, L. D. Improving CAR-T immunotherapy: Overcoming the challenges of T cell exhaustion. *EBioMedicine* **77**, 103941 (2022).
68. Zhao, Y. et al. IL-10-expressing CAR T cells resist dysfunction and mediate durable clearance of solid tumors and metastases. *Nat. Biotechnol.* (2024).
69. Li, X. et al. Suppression of cytokine release syndrome during CAR-T-cell therapy via a subcutaneously injected interleukin-6-adsorbing hydrogel. *Nat. Biomed. Eng.* **7**, 1129–1141 (2023).
70. Kim, M. Y. et al. A long-acting interleukin-7, rhIL-7-hyFc, enhances CAR T cell expansion, persistence, and anti-tumor activity. *Nat. Commun.* **13**, 3296 (2022).
71. Liu, D. et al. Tumor microenvironment-responsive nanoparticles amplifying STING signaling pathway for cancer immunotherapy. *Adv. Mater.* **36**, e2304845 (2024).
72. Chen, X. et al. Chemically programmed STING-activating nanoliposomal vesicles improve anticancer immunity. *Nat. Commun.* **14**, 4584 (2023).
73. Cao, L. L. & Kagan, J. C. Targeting innate immune pathways for cancer immunotherapy. *Immunity* **56**, 2206–2217 (2023).
74. Tang, L. et al. Extracellular vesicles-derived hybrid nanoplatforms for amplified cd47 blockade-based cancer immunotherapy. *Adv. Mater.* **35**, e2303835 (2023).

75. Lai, J. et al. Triple hybrid cellular nanovesicles promote cardiac repair after ischemic reperfusion. *ACS Nano* **18**, 4443–4455 (2024).
76. Mondal, J. et al. Hybrid exosomes, exosome-like nanovesicles and engineered exosomes for therapeutic applications. *J. Control Release* **353**, 1127–1149 (2023).
77. Cheng, Q. et al. Genetically engineered-cell-membrane nanovesicles for cancer immunotherapy. *Adv. Sci. (Weinh)* **10**, e2302131 (2023).
78. Liang, Y., Duan, L., Lu, J. & Xia, J. Engineering exosomes for targeted drug delivery. *Theranostics* **11**, 3183–3195 (2021).
79. Kimiz-Gebologlu, I. & Oncel, S. S. Exosomes: Large-scale production, isolation, drug loading efficiency, and biodistribution and uptake. *J. Control Release* **347**, 533–543 (2022).
80. Zheng, Z., Chinnasamy, N. & Morgan, R. A. Protein L: a novel reagent for the detection of chimeric antigen receptor (CAR) expression by flow cytometry. *J. Transl. Med.* **10**, 29 (2012).
81. Zhang, X. et al. Depletion of BATF in CAR-T cells enhances antitumor activity by inducing resistance against exhaustion and formation of central memory cells. *Cancer Cell* **40**, 1407–1422 e1407 (2022).
82. Wang, Y. et al. Low-dose decitabine priming endows CAR T cells with enhanced and persistent antitumour potential via epigenetic reprogramming. *Nat. Commun.* **12**, 409 (2021).
83. Tang, N. et al. TGF-beta inhibition via CRISPR promotes the long-term efficacy of CAR T cells against solid tumors. *JCI Insight* **5**, e133977 (2020).

Acknowledgements

This work was supported by grants from the National Natural Science Foundation of China (82072062 (X.H.), 82272388 (G.J.), 82072365 (G.J.) and 82303799 (T.Z.)), the National Science and Technology Key Projects for Major Infectious Diseases (2017ZX10302301-002 (X.H.)), and the Development Project of Foshan Fourth People's Hospital (FSSYKF-2020003 (X.H.) and FSSYKF-2020017 (X.H.)).

Author contributions

Conceptualization: T.Z., Y.X., Methodology: Y.X., T.Z., Z.C., H.D., Investigation: T.Z., Y.X., Funding acquisition: X.H., T.Z., G.J., Project administration: X.H., Supervision: X.H., S.C., G.J., Writing – original draft: T.Z., Y.X., Writing – review & editing: X.H., S.C., G.J., T.Z.

Competing interests

The authors declare no competing interests.

Additional information

Supplementary information The online version contains supplementary material available at https://doi.org/10.1038/s41467-024-55751-4.

Correspondence and requests for materials should be addressed to Shoudeng Chen, Guanmin Jiang or Xi Huang.

Peer review information *Nature Communications* thanks Alexander Kamb, Peng Li and the other, anonymous, reviewer(s) for their contribution to the peer review of this work. A peer review file is available.